

Comparison of algorithms for solving the sign problem in the O(3) model in 1+1 dimensions at finite chemical potential

S. Katz^{1,2}, F. Niedermayer³, D. Nógrádi^{1,2}, Cs. Török^{1,2}

¹ *Institute for Theoretical Physics, Eötvös University,
Pázmány Péter sétány 1/A, H-1117 Budapest, Hungary*

² *MTA-ELTE "Lendület" Lattice Gauge Theory Research Group,
Pázmány Péter sétány 1/A, H-1117 Budapest, Hungary*

³ *Institute for Theoretical Physics,
Albert Einstein Center for Fundamental Physics Bern University,
Sidlerstrasse 5, CH-3012 Bern, Switzerland*

(Dated: June 18, 2022)

We study three possible ways to circumvent the sign problem in the O(3) nonlinear sigma model in 1+1 dimensions. We compare the results of the worm algorithm to complex Langevin and multi-parameter reweighting. Using the worm algorithm, the thermodynamics of the model is investigated, continuum results are shown for the pressure at different μ/T values in the range 0–4. By performing $T = 0$ simulations using the worm algorithm the Silver Blaze phenomenon is reproduced. Regarding complex Langevin, we test various implementations of discretizing the complex Langevin equation. We found that the exponentialized Euler discretization of the Langevin equation gives wrong results for the action and the density at low T/m . By performing continuum extrapolation we found that this discrepancy does not disappear and depends slightly on temperature. The discretization with spherical coordinates perform similarly at low μ/T , but goes wrong also at some higher temperatures at high μ/T . However, a third discretization that uses a constraining force to achieve the $\phi^2 = 1$ condition gives correct results for the action, but wrong results for the density at low μ/T .

I. INTRODUCTION

Monte Carlo simulations of quantum field theories based on the path integral formalism play an important role in investigating the physics of various models nonperturbatively. However, standard numerical methods fail when the action becomes complex, and thus the probability interpretation of the weight e^{-S} , and importance sampling can not be applied. The problem is present in QCD at finite density or with a theta term, and also arises in condensed matter physics, e.g. in the simulations of strongly correlated electronic systems [1]. To solve these complex action problems, several methods have been devised, for a review of different approaches and further references, see [2–5].

In the present paper, we compare and test three different methods, namely reweighting, worm algorithm and complex Langevin in the case of the 1+1 dimensional O(3) model. Our focus is primarily on the applicability of the complex Langevin algorithm, since today it may seem that it is a promising approach to simulate even QCD [6, 7], although several problems have not been solved yet. The idea behind complex Langevin is stochastic quantisation and originates from the work of Parisi, Wu and Klauder from the 80's [17–19]. But soon after its proposal, the first simulations revealed certain problems: the instability of the simulations with absence of convergence (runaway trajectories) [20], and that even stable simulations may converge to a wrong limit [21]. These problems hindered reliable calculations, but in the last decade important improvements have been achieved. Runaway trajectories can now be eliminated e.g. using adaptive stepsize [22], and a formal justification of

the algorithm, as well as necessary and sufficient conditions for convergence to correct results have been established [23–25]. Roughly speaking, these suggest that if the probability distributions of the complexified variables fall sufficiently fast, then the results are correct. In order to reach this for gauge theories, the gauge cooling procedure was developed [26], which works perfectly in some models or at a certain parameter range, but may fail in other models and parameter ranges [26–29]. In [29] – where heavy dense QCD (HDQCD) was studied –, it was argued that failure happens below a specific β value and by increasing the temporal lattice size, one can get correct results at lower temperatures, in other words continuum extrapolation may be feasible. The validity of this statement however is not entirely clear and may be model dependent. On the one hand, the above observation in HDQCD helped to explore the phase diagram of the model [30], but on the other hand in the case of full QCD, recent results [7] show that using $N_t = 4, 6, 8$ lattices, the breakdown of complex Langevin prevents the exploration of the confined region. We note, that e.g. for the 3d XY model the breakdown of complex Langevin also occurred around the phase boundary [31], but in that model the question of continuum limit behaviour can not be addressed.

In the present paper, we investigate the 1+1 dimensional O(3) model for this purpose, which is not a gauge theory, but asymptotically free, thus the continuum behaviour can be analyzed. We compare the results of different discretizations of the complex Langevin equation to the results of reweighting and the worm algorithm.

From the viewpoint of the sign problem, these two approaches are also interesting and can give insight into the

properties of the O(3) model.

In this sense, reweighting is a well-defined approach, but with limited efficiency and reliability as the sign problem becomes more severe (and also overlap problems appearing). The worm algorithm or also called dual variables approach [32] however completely eliminates the sign problem of the model by introducing new, dual variables. The difficulty in this case is the rewriting of the model to these dual variables, but after it has been accomplished, effective simulations using the worm algorithm can be performed, and in fact many interesting models were studied during the years [33–40]. Here, using the worm algorithm we study the thermodynamic properties of the O(3) model.

Although the dual formalism of this model was introduced and studied [41, 42] during the finalization of our work on the comparison of the different methods, we also introduce this formalism in this paper in order to give a consistent introduction to our notations.

In the following sections, after some introductory remarks about the O(3) model in Sec. II and the description of scale setting in Sec. III, we discuss these approaches in more detail, in Sec. IV the reweighting, in Sec. V the worm algorithm and in Sec. VI the complex Langevin. In Sec. VII we compare the results of the simulations. In the Appendix we discuss in detail the updating steps of the worm algorithm.

II. FORMULATION

The O(3) model in 1+1 dimensions has been widely studied in the past for several reasons, amongst others because it has interesting features in common with four-dimensional non-Abelian gauge theories. Over the years, many important results have been achieved also numerically and - since the model is more or less tractable - analytically. Nonetheless, we do not overview here the overall history of these results, but mention only some facts that made this model attractive for us.

First of all, the coupling constant of the theory is dimensionless, thus the theory is perturbatively renormalisable. It is asymptotically free in 1+1 dimensions [8, 9], which enables us to study the continuum limit of the results obtained at finite lattice spacings. The O(3) model also has a nonperturbative mass gap generated dynamically due to interactions. Moreover, similarly to QCD, the O(3) model also possesses instanton solutions [15, 16].

The Lagrangian of the nonlinear O(3) model is

$$\mathcal{L} = \frac{1}{2g^2} (\partial_\mu \phi)^2, \quad (1)$$

where the fields obey the $\sum_{i=1}^3 \phi_i^2 = 1$ condition in every spacetime point.

The discretized action in 1+1 dimensions with periodic

boundary condition is

$$\begin{aligned} S &= \frac{1}{g^2} \left(2 \sum_x \phi_x^2 - \sum_{x,\mu=0,1} \phi_{x+\hat{\mu}} \phi_x \right) \\ &= 2\beta V - \beta \sum_{x,\mu=0,1} \phi_{x+\hat{\mu}} \phi_x, \end{aligned} \quad (2)$$

where we introduced $\beta = 1/g^2$ and the lattice volume $V = N_x \times N_t$. After introducing chemical potential to the rotations in the (12)-plane of O(3), the action becomes

$$S = 2\beta V - \beta \sum_x (\phi_{x+\hat{0}} e^{i\mu a t_{12}} \phi_x + \phi_{x+\hat{1}} \phi_x), \quad (3)$$

where t_{12} is the generator of the rotation in the (12)-plane of O(3).

III. SCALE SETTING

Since in the later part of the paper we are interested in continuum extrapolations and physical quantities computed from the dimensionless quantities measured on the lattice, we need to determine the lattice spacing as a function of β , which we discuss in this Section. In order to achieve this, $\mu = 0$ simulations have been performed, for which we used the cluster algorithm [10–12], and measured the second moment correlation length ξ_2 at zero temperature. ξ_2 is defined through

$$\frac{1}{\xi_2} = \frac{\sin(\pi/N_t)}{\pi/N_t} \sqrt{\left(\frac{2M_0 a^2}{M_2} - \frac{4\pi^2}{N_t^2} \right)}, \quad (4)$$

where M_0 denotes the zeroth and M_2 the second moment [43, 44]:

$$M_{2n} = \left(\frac{N_t a}{2\pi} \right)^{2n} \sum_t \left(2 \sin \left(\frac{\pi t}{N_t a} \right) \right)^{2n} C(t). \quad (5)$$

$C(t)$ is the 2-point correlation function, $C(t) = \sum_x \langle \sum_a \phi_a(x, t) \phi_a(0, 0) \rangle$. ξ_2 does not equal to $\xi = 1/ma$ but scales as ξ in the $\beta \rightarrow \infty$ limit [43, 45, 46] and in infinite volume the ratio ξ/ξ_2 is very close to 1, it is 1.000826(1) [47]. The advantage of using ξ_2 is that one does not need to fit any correlators this way. We can thus estimate the mass gap $ma = 1/\xi$ with the help of ξ_2 by running large volume, zero temperature simulations. Actually, we used 80×80 and 100×100 lattices for $0.9 \leq \beta \leq 1.57$, 120×120 and 140×140 lattices for $1.58 \leq \beta \leq 1.62$, 250×250 lattices for $1.63 \leq \beta \leq 1.72$, and 400×400 lattices for $1.73 \leq \beta \leq 1.85$. The simulation points were chosen uniformly in the above β ranges with $\Delta\beta = 0.01$ distance from each other with 10^6 or 2×10^6 cluster updates after thermalization, using every 10th for measurement. We studied the overlapping β regions as well, and used larger lattices if deviations larger than errors between the smaller and larger volumes have occurred. The results are shown in Fig. 1.

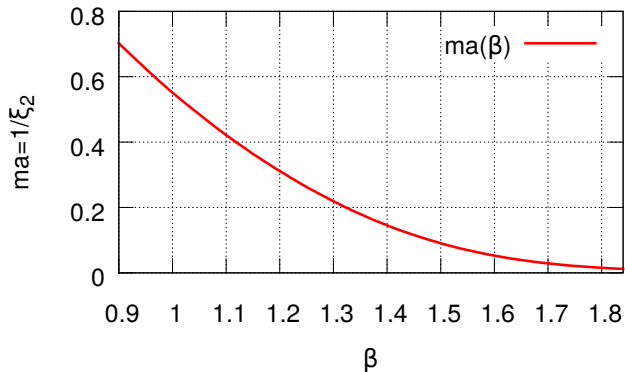


FIG. 1. The $ma(\beta)$ scale for the 1+1 dimensional $O(3)$ model. (Errors are smaller or compatible with the width of the line.) The parameters and details of the simulations are summarized in the text.

IV. REWEIGHTING

Rewighting uses the idea of rewriting the partition function (and the expectation value of observables) in such a way, that one needs to do simulations only at zero μ and determine the configurations that can be relevant at finite μ . This is done by measuring the weights of the configurations, which enables one to distinguish between them.

In the multi-parameter reweighting approach [48], one reweights both in β and μ , as we show it for the partition function of the $O(3)$ model:

$$\begin{aligned} Z &= \int \prod_x d\phi_x \delta(\phi_x^2 - 1) e^{-S(\beta, \mu)} \\ &= \int \prod_x d\phi_x \delta(\phi_x^2 - 1) e^{-S(\beta_0, \mu_0=0)} w(\beta, \mu, \beta_0, \mu_0=0) \\ &= Z_0 \langle w \rangle_{\beta_0, \mu_0=0}, \end{aligned} \quad (6)$$

where $w(\beta, \mu, \beta_0, \mu_0=0) = e^{S(\beta_0, \mu_0=0) - S(\beta, \mu)}$ is the weight and Z_0 is the partition function for β_0 and $\mu_0=0$. As one can see, this rewritten partition function can be simulated directly using standard methods since the action $S(\beta_0, \mu_0=0)$ is real. Using reweighting the expectation value of an O observable is the following:

$$\langle O(\beta, \mu) \rangle_{\beta, \mu} = \frac{\langle O(\beta, \mu) w(\beta, \mu, \beta_0, \mu_0=0) \rangle_{\beta_0, \mu_0=0}}{\langle w(\beta, \mu, \beta_0, \mu_0=0) \rangle_{\beta_0, \mu_0=0}}. \quad (7)$$

Although reweighting can reduce the sign problem, overlap problems occur in this case. That is we have different important configurations at our 'source' ($\beta_0, \mu=0$) ensemble and at the 'target' (β, μ) ensemble. If the two sets just slightly overlap or do not overlap at all, then one rarely reaches the important configurations at β, μ by simulating at $\beta_0, \mu_0=0$.

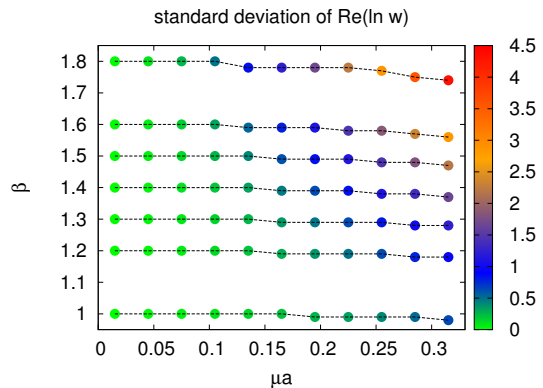


FIG. 2. The standard deviation of $\text{Re}(\ln w)$ for reweighting from $\beta_0 = 1, 1.2, 1.3, 1.4, 1.5, 1.6, 1.8$ to different β, μ values on 56×14 lattices. We define the best reweighting lines (with dashed) as those that have the smallest standard deviations on them.

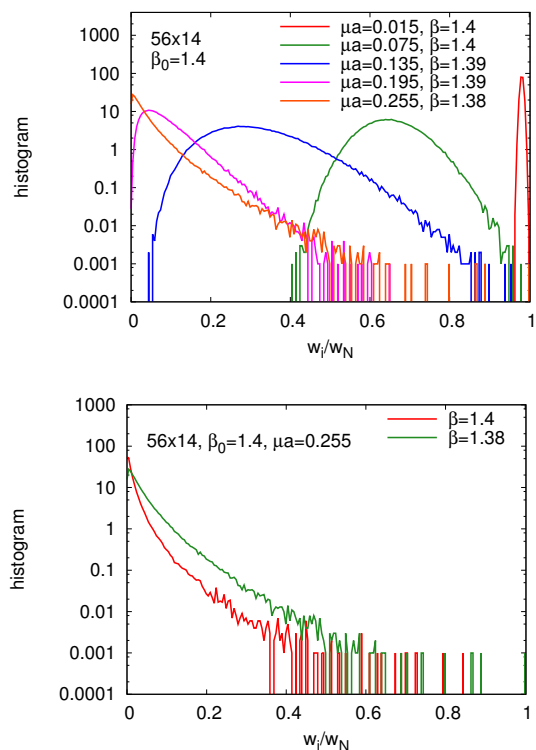


FIG. 3. Top: The histogram of normalized weights along the best reweighting line starting from $\beta_0 = 1.4, \mu_0 = 0$ shows the severeness of the overlap problem. At the horizontal axis, one finds w_i/w_N , where w_i s are the absolute values of the weights sorted as $w_1 < w_2 \dots < w_N$, while at the vertical axis we show $\# / N / \Delta w$, where $\#$ is the number of configurations that have normalized weights between w_i/w_N and $w_i/w_N + \Delta w$. N is the total number of configurations and $\Delta w = 0.005$. Bottom: The figure illustrates how reweighting in β can help to enhance overlapping: the green curve shows that one has more configurations with greater weights when reweighting from $\beta_0 = 1.4, \mu_0 a = 0$ to $\beta = 1.38, \mu a = 0.255$, than in the case of e.g. standard reweighting.

In these cases it can happen that one has many relatively small weights at the same order of magnitude, and only some with many magnitudes larger, and as a consequence collects only a tiny fraction of useful statistics during even long simulations. It was observed that multi-parameter reweighting helps to reduce the overlap problem in the case of QCD, and also can help to reduce the sign problem by doing reweighting on the so called 'best reweighting lines' [49, 50]. These are defined as those curves that have the smallest standard deviations of $\text{Re}(\ln w)$ on them. In the case of the $O(3)$ model we illustrate these lines in Fig. 2 and we show the overlap problem and the advantages of multi-parameter reweighting in Fig. 3, top and bottom panel, respectively. We also illustrate the severeness of the sign problem in Figure 4, which is based on measurements on 56×14 lattices. We used the cluster algorithm to simulate at $\mu_0 = 0$. Further results obtained by the multi-parameter reweighting method can be found in Sec. VII, where we compare them to the worm and complex Langevin results.

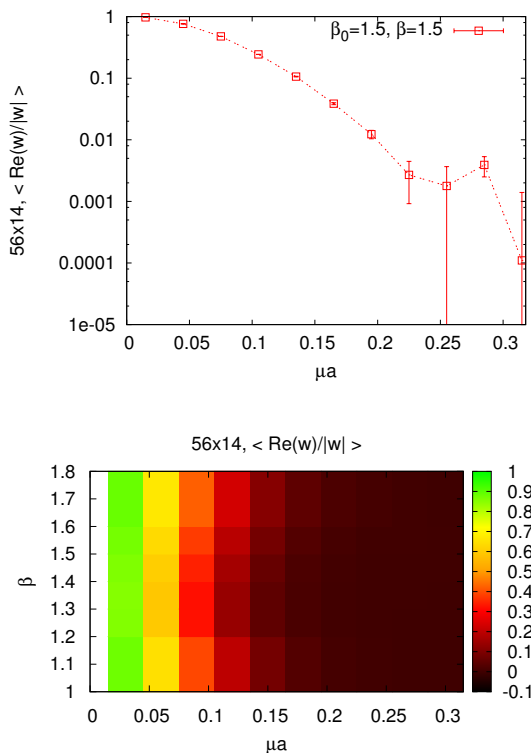


FIG. 4. Top: The figure shows the expectation value of the real part of the normalized weight at 56×14 lattice when reweighting from $\beta_0 = 1.5, \mu_0 = 0$ to $\beta = 1.5$ and μa values along the horizontal axis. Bottom: $\langle \text{Re}(w)/|w| \rangle$ shows how hard is the sign problem in different β, μ regions.

V. THE WORM ALGORITHM

Another approach we employed in this study is the worm algorithm. In order to maintain generality we will

review the algorithm and the dual formulation in the $O(N)$ case at $d + 1$ dimension. In the $O(N)$ case, the fields obey the $\sum_{i=1}^N \phi_i^2 = 1$ condition in every spacetime point. The discretized action in $d + 1$ dimensions is

$$S = \beta(d+1)V_{d+1} - \beta \sum_x (\phi_{x+\hat{0}} e^{i\mu a t_{12}} \phi_x + \sum_{i=1, \dots, d} \phi_{x+\hat{i}} \phi_x), \quad (8)$$

where now $\beta = a^{d-1}/g^2$ and the $d + 1$ dimensional lattice volume is $V_{d+1} = N_s^d \times N_t$.

Our goal in lattice simulations is to calculate expectation values. The worm algorithm performs this as counting different types of configurations, as we are going to explain it later. The algorithm itself is based on the dual formulation of a model, which means in our case the characterization of configurations not with the $\phi(x)$ continuous variables at every lattice point, but with a set of discrete variables $\{m_a\}_{a=(l; i=1, \dots, N)}$, which 'live' on links (l). One $\{m_a\}$ configuration matches to a certain, finite partial sum of an infinite sum (e.g. the expansion of the partition sum), and the algorithm jumps between these partial sums.

In the following, we first review some conventional notations and integrals over the $O(N)$ sphere, which is helpful for the derivation of weights. Then, at first, we restrict ourselves for the dual formulation of the case without chemical potential and introduce the worm algorithm, then we repeat the same procedure for the case with chemical potential. Finally we present continuum results in Subsections VD 1, VD 3, and comparisons to reweighting and complex Langevin can be found in Sec. VII.

A. Integrals over $O(N)$ sphere

Consider an $O(N)$ vector ϕ of unit length, $\phi^2 = 1$. Averaging over $O(N)$ sphere, with the normalization condition $\langle 1 \rangle = 1$, one has $\langle \phi_i \phi_j \rangle = \delta_{ij}/N$, $\langle \phi_i \phi_j \phi_k \phi_l \rangle = (\delta_{ij} \delta_{kl} + \delta_{ik} \delta_{jl} + \delta_{il} \delta_{jk}) / (N(N+2))$. For the general case of k even number of vectors one has

$$\langle \phi_{i_1} \phi_{i_2} \dots \phi_{i_k} \rangle = C_k^{(N)} (\delta_{i_1 i_2} \delta_{i_3 i_4} \dots \delta_{i_{k-1} i_k} + \text{perm}), \quad (9)$$

where

$$C_k^{(N)} = \frac{1}{N(N+2) \dots (N+k-2)} = \frac{\Gamma(N/2)}{2^{k/2} \Gamma(N/2 + k/2)}. \quad (10)$$

In the brackets in (9) there are altogether

$$M_k = (k-1)!! \equiv 1 \cdot 3 \cdot \dots \cdot (k-3)(k-1) = 2^{-\frac{k}{2}+1} \frac{\Gamma(k)}{\Gamma(k/2)} \quad (11)$$

terms for all possible pairings of the indices. This can be obtained e.g. from the recursion relation $M_{k+2} = M_k + k(k-1)M_{k-2}$, with $M_2 = 1, M_4 = 3$. To check this, one can contract in the last two indices i_{k-1}, i_k .

The corresponding recursion relation reads

$$C_{k-2}^{(N)} = C_k^{(N)} \left(N + \frac{M_k}{M_{k-2}} - 1 \right) = C_k^{(N)} (N + k - 2). \quad (12)$$

It is interesting to note that for a free system, i.e. when the constraint $\delta(\phi^2 - 1)$ is replaced by the Gaussian $\exp(-\phi^2/2)$ then one gets $C_k^{(N)} = 1$ for the weights in (9). This is in agreement with the relation

$$\lim_{N \rightarrow \infty} N^{k/2} C_k^{(N)} = \lim_{N \rightarrow \infty} \frac{N^{k/2}}{N(N+2)\dots(N+k-2)} = 1. \quad (13)$$

When one collects the powers of different components one has

$$\begin{aligned} w(k_1, \dots, k_N) &\equiv \langle \phi_1^{k_1} \phi_2^{k_2} \dots \phi_N^{k_N} \rangle \\ &= \frac{\Gamma(N/2)}{\Gamma((k+N)/2)} \prod_{i=1}^N \frac{\Gamma((k_i+1)/2)}{\Gamma(1/2)} \\ &= \frac{1}{N(N+2)\dots(N+k-2)} \prod_{i=1}^N (1 \cdot 3 \cdot \dots \cdot (k_i - 1)), \end{aligned} \quad (14)$$

where all k_i are even and $k = k_1 + \dots + k_N$. In the last expression the product is taken only for i 's for which $k_i > 0$. Also, obviously, $w(0, 0, \dots, 0) = 1$. Some useful relations obtaining the coefficients are (assuming that all powers k are even):

$$\int_{-\infty}^{\infty} dx e^{-x^2} x^k = \Gamma\left(\frac{k+1}{2}\right), \quad (15)$$

and

$$\begin{aligned} \int d^N x e^{-x^2} x_1^{k_1} \dots x_N^{k_N} &= \prod_{i=1}^N \Gamma\left(\frac{k_i+1}{2}\right) \\ &= \int_0^\infty e^{-r^2} r^{N+k-1} S_N \langle \phi_1^{k_1} \dots \phi_N^{k_N} \rangle \\ &= \frac{1}{2} \Gamma\left(\frac{N+k}{2}\right) S_N \langle \phi_1^{k_1} \dots \phi_N^{k_N} \rangle, \end{aligned} \quad (16)$$

where S_N is the surface of the N -dimensional sphere: $S_N = 2\pi^{N/2}/\Gamma(N/2)$.

B. Strong coupling expansion without chemical potential

In the case without chemical potential, for one link between neighbor lattice points x and y , one can write

$$\begin{aligned} e^{\beta\phi(x)\phi(y)} &= \sum_{m_1, \dots, m_N} \frac{\beta^m}{m_1! \dots m_N!} (\phi_1(x)\phi_1(y))^{m_1} \dots \\ &\quad \times (\phi_N(x)\phi_N(y))^{m_N}, \end{aligned} \quad (17)$$

where $m = m_1 + \dots + m_N$. Then one can consider the sum

$$\begin{aligned} \sum_{i=1}^N \sum_{u, v \in \Lambda} \int_{\phi} \phi_i(u)\phi_i(v) e^{-S} &= \sum_{\text{conf}} W(u, v, i; m) \\ &= e^{-\beta(d+1)V_{d+1}} \sum_{\text{conf}} \left(\prod_l \frac{\beta^{m^{(l)}}}{m_1^{(l)}! \dots m_N^{(l)}!} \right) \\ &\quad \times \left(\prod_x w(k_1(x), \dots, k_N(x)) \right), \end{aligned} \quad (18)$$

where $\text{conf} = \{u, v, i; \{m_j^{(l)}\}_{j=1, \dots, N}^{\text{all } l \text{ links}}\}$ is the configuration: two distinguished points (u and v), a component i , and the set $\{m_j^{(l)}\}_{j=1, \dots, N}^{\text{all } l \text{ links}}$. During the simulations the configuration can change in different ways, which we discuss in the Appendix. One way is to change u to a neighboring site and meanwhile increasing/decreasing $m_i^{(l)}$ along the l link that connects these two. We start from $u = v$ and the continuous path connecting u and v that appears this way is called the *worm*. The weights $w(\dots)$ of Eq. (18) are given by Eq. (14). The value of $k_j(x)$ depends on the position of x : $k_j(x) = \hat{k}_j(x) + (\delta_{xu} + \delta_{xv})\delta_{ij}$, where $\hat{k}_j(x) = \sum_{x \in \partial l} m_j^{(l)}$. Then all $k_j(x)$ values must be even.

The ratios of the weights when one of the k_i 's changed by ± 2 are

$$\frac{w(k_1 + 2, k_2, \dots, k_N)}{w(k_1, k_2, \dots, k_N)} = \frac{k_1 + 1}{k_1 + N}, \quad (19)$$

$$\frac{w(k_1 - 2, k_2, \dots, k_N)}{w(k_1, k_2, \dots, k_N)} = \frac{k_1 - 1}{k_1 - 1}. \quad (20)$$

With the help of the sum (18) defined above, one can see that the partition sum is related to those configurations where the two ends of the worm coincides ($u = v$), this gives explicitly $V_{d+1}Z$. The configurations with one distance between the two ends (c_1) divided by the number of configurations where the two ends of the worm coincides (c_2), gives $\frac{c_1}{c_2} = -\frac{2}{\beta} \left(\frac{\langle S \rangle}{V_{d+1}} - \beta(d+1) \right)$, from which one can determine $\langle S \rangle$, the expectation value of the action.

C. Strong coupling expansion with chemical potential

The action with chemical potential coupled to t_{12} is obtained from the standard one by replacing the interaction terms which couple the fields in the time direction according to $\phi(x+\hat{0})\phi(x) \rightarrow \phi(x+\hat{0})e^{i\mu at_{12}}\phi(x)$. Therefore, the corresponding action is complex. For the O(2) non-linear sigma-model this problem was avoided in [34] using the worm algorithm: the terms in the strong-coupling expansion are real even in the presence of the chemical potential. We describe here the extension to the O(N) case

for general N . Let us introduce $\phi_{\pm} = \frac{1}{\sqrt{2}}(\phi_1 \pm i\phi_2)$. Expressed through these variables the scalar product is

$$\begin{aligned} \phi(x + \hat{0})\phi(x) &= \phi_-(x + \hat{0})\phi_+(x) + \phi_+(x + \hat{0})\phi_-(x) \\ &+ \phi_3(x + \hat{0})\phi_3(x) + \dots + \phi_N(x + \hat{0})\phi_N(x) \end{aligned} \quad (21)$$

and the action is

$$\begin{aligned} S &= \beta(d+1)V_{d+1} - \beta \sum_x \sum_{\nu=0}^d \left(e^{-\mu\nu a} \phi_-(x + \hat{\nu})\phi_+(x) \right. \\ &+ \left. e^{\mu\nu a} \phi_+(x + \hat{\nu})\phi_-(x) + \sum_{j=3}^N \phi_j(x + \hat{\nu})\phi_j(x) \right), \end{aligned} \quad (22)$$

where $\mu_\nu = \mu\delta_{\nu,0}$, $\nu = 0, 1, \dots, d$. When one integrates over ϕ at a given site, the non-vanishing contributions are all real and positive:

$$\begin{aligned} w(k_1, k_2, \dots, k_N) &= \langle (\phi_+ \phi_-)^{k_{12}} \phi_3^{k_3} \dots \phi_N^{k_N} \rangle \\ &= \frac{1}{2^{k_{12}}} \sum_{m=0}^{k_{12}} \binom{k_{12}}{m} \langle \phi_1^{2m} \phi_2^{2k_{12}-2m} \phi_3^{k_3} \dots \phi_N^{k_N} \rangle \\ &= \frac{\Gamma(N/2)}{\Gamma((k+N)/2)} 2^{-k_{12}} \Gamma(k_{12} + 1) \prod_{i=3}^N \frac{\Gamma((k_i + 1)/2)}{\Gamma(1/2)}, \end{aligned} \quad (23)$$

where $k = 2k_{12} + k_3 + \dots + k_N$ and k_3, \dots, k_N are even.

The strong coupling expansion for spatial neighbor sites are the same as in (17), and for temporal neighbor sites it is

$$\begin{aligned} e^{\beta \mathbf{S}^T e^{i\mu a t_{12}} \mathbf{S}'} &= \sum_{m_+, m_-, m_3, \dots, m_N} \frac{\beta^m}{m_+! m_-! m_3! \dots m_N!} \\ &\times (e^{\mu a} S_- S'_+)^{m_+} (e^{-\mu a} S_+ S'_-)^{m_-} (S_3 S'_3)^{m_3} \dots (S_N S'_N)^{m_N}, \end{aligned} \quad (24)$$

where $m = m_+ + m_- + m_3 + \dots + m_N$ and $\mathbf{S} \equiv \phi(x)$, $\mathbf{S}' \equiv \phi(x + \hat{0})$. Consider then

$$\begin{aligned} \sum_i \sum_{u, v \in \Lambda} \int_{\phi} \phi_i(u) \phi_i(v) e^{-S} &= \sum_{\text{conf}} W(\{u, v, i; m\}; \mu) \\ &= e^{-\beta(d+1)V_{d+1}} \sum_{\text{conf}} \left(\prod_l \frac{\beta^{m^{(l)}} e^{(\mu a)^{(l)} m_+^{(l)}} e^{-(\mu a)^{(l)} m_-^{(l)}}}{m_+^{(l)}! m_-^{(l)}! \dots m_N^{(l)}!} \right) \\ &\times \left(\prod_x w(k_{12}(x), k_3(x), \dots, k_N(x)) \right), \end{aligned} \quad (25)$$

where $i = +, -, 3, \dots, N$, and $(a\mu)^{(l)} = a\mu$ for time-like links, and 0 for spatial links. In these expressions

$$k_j(x) = \hat{k}_j(x) + \delta_{xu} \delta_{j i_u} + \delta_{xv} \delta_{j i_v} \quad j = +, -, 3, \dots, N, \quad (26)$$

where $(i_u, i_v) = (-, +), (3, 3), \dots, (N, N)$, and different \hat{k} 's are defined as

$$\hat{k}_+(x) = \sum_{\nu=0}^d \left(m_+^{(x-\hat{\nu}, x)} + m_-^{(x, x+\hat{\nu})} \right) \quad (27)$$

$$\hat{k}_-(x) = \sum_{\nu=0}^d \left(m_-^{(x-\hat{\nu}, x)} + m_+^{(x, x+\hat{\nu})} \right) \quad (28)$$

$$\hat{k}_j(x) = \sum_{x \in \partial l} m_j^{(l)} = \sum_{\nu=0}^d \left(m_j^{(x, x+\hat{\nu})} + m_j^{(x-\hat{\nu}, x)} \right) \quad j = 3, \dots, N \quad (29)$$

The non-zero terms in (25) are those where the same number of $\phi_+(x)$ and $\phi_-(x)$ factors are present, i.e. $k_+(x) = k_-(x) = k_{12}$ and the number of $\phi_j(x)$ factors, $k_j(x)$ (for $j = 3, \dots, N$) is even at all sites x . The detailed steps of the worm algorithm based on these prescriptions are discussed in the Appendix. In the following Subsections we leave the general formalism and consider the O(3) model in 1 + 1 dimensions.

D. Numerical results obtained with the worm algorithm

1. Pressure

Similar to as was mentioned at the end of Subsection VB, the (25) sum is related to the partition function if $u = v$, when it gives $V_2 Z$. For the action, one needs to calculate the ratio of two terms. In the denominator there is Z , while in the numerator there is $-\frac{\beta}{2}(e^{\mu a} \times \#_1 + e^{-\mu a} \times \#_2 + \#_3 + \#_4)$, where $\#_1$ is the number of configurations with $v = u + \hat{0}$ and $i_u = -, i_v = +$; $\#_2$ is the number of configurations with $u - \hat{0} = v$ and $i_u = -, i_v = +$; $\#_3$ is the number of configurations with $u \pm \hat{1} = v$ and $i_u = -, i_v = +$; and $\#_4$ is the number of configurations with $u \pm \hat{\nu} = v$ with $\nu = 0, 1$ and $i_u, i_v = 3$. The value of the numerator is constructed the way that is suitable for the action (22). (The first term of (22), which is independent of the dual variables was added to the averages at the end.)

For calculating thermodynamic quantities we used lattices with $N_x > N_t$, and measured the action after each worm movement. Since it is divergent as $a \rightarrow 0$, we renormalized it using $\langle S(\beta, T = 0, \mu = 0) \rangle$. For the latter we used large symmetric lattices, in particular those that were used to determining the scale (see Sec. III). In order to eliminate the finite-size effects, we chose box sizes of $ma(\beta_{pc})N_x \geq 5$, where β_{pc} is the inflection point of the pressure (or in other words the location of the maximum of the renormalized action divided by β). This β_{pc} is only a pseudo-critical quantity and does not correspond to any phase transition, since no phase transition occurs due to the spontaneous breaking of the global O(3) symmetry in the two dimensional O(3) model, according to the Mermin–Wagner–Coleman theorem [13, 14]. The chosen box sizes correspond to the aspect ratio $N_x/N_t = 4$, so we have used $32 \times 8, 40 \times 10, 56 \times 14, 64 \times 16, 72 \times 18, 80 \times 20, 120 \times 30$ lattices for finite temperature simulations.

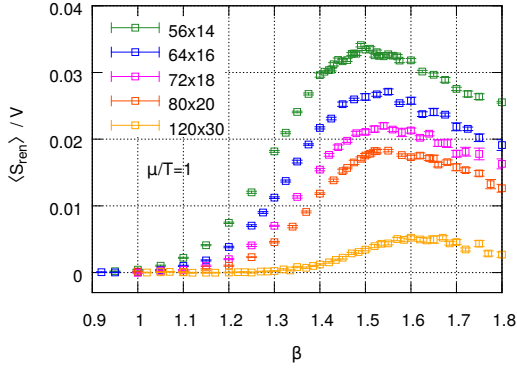


FIG. 5. The renormalized action divided by the lattice volume ($V = N_x \times N_t$), measured by the worm algorithm.

We used around $4 \times 10^{10} \dots 1.2 \times 10^{11}$ local worm updates on these lattices, after $(3 \dots 5) \times 10^5$ thermalization steps. Note that these numbers refer to the local change of the configuration. In order to compare the amount of updates to those of the Langevin simulations, one should divide them with the two dimensional lattice volume. After calculating the action, we used the *integral method* [52] to obtain the pressure $p(T)$:

$$\begin{aligned} \frac{p}{T^2} &= \frac{N_t}{N_x} \log Z = \frac{N_t}{N_x} \int_{\beta_0}^{\beta} d\beta' \frac{\partial \log Z}{\partial \beta'} \\ &= \frac{N_t}{N_x} \int_{\beta_0}^{\beta} d\beta' \left\langle -\frac{\partial S}{\partial \beta'} \right\rangle. \end{aligned} \quad (30)$$

Since we defined S with β included, $\partial S / \partial \beta$ is simply S / β . The pressure is also divergent, so we need to renormalize it using the expectation value of the renormalized action $\langle S_{ren}(\beta, T, \mu) \rangle = \langle S(\beta, T, \mu) \rangle - \langle S(\beta, T = 0, \mu = 0) \rangle$ in the integrand of formula (30). In the following we denote the renormalized pressure with p . Figure 5 shows the renormalized action density at $\mu/T = 1$, while figures 6 and 7 shows the results for the renormalized pressure.

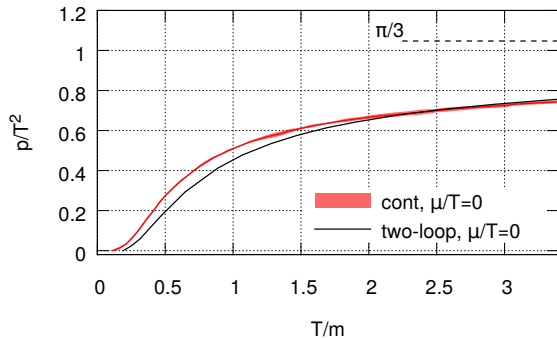


FIG. 6. Comparison of our lattice results and the two-loop calculation of [53] for p/T^2 at $\mu = 0$ in the continuum. The dashed line at $\pi/3$ shows the asymptotic limit at high temperature.

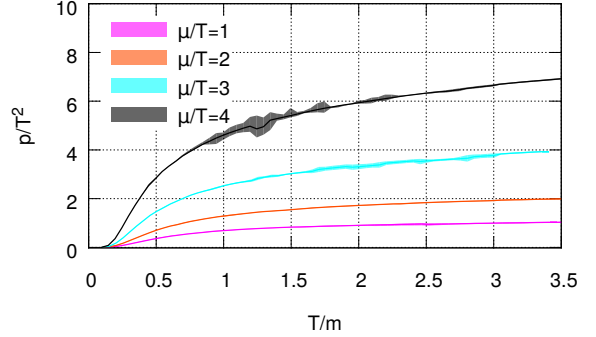
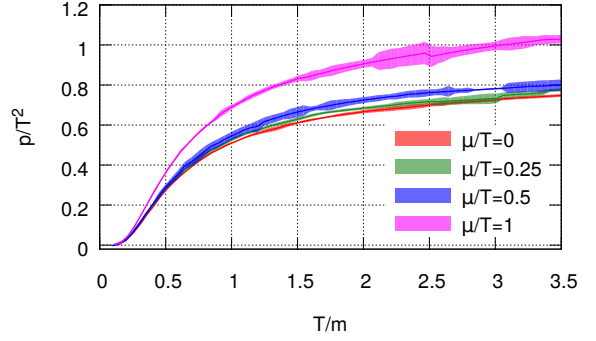


FIG. 7. Continuum results for p/T^2 as a function of T/m for different μ/T values.

2. Trace anomaly

Another quantity of interest is the trace anomaly (or also called interaction measure):

$$\frac{\theta}{T^2} = \frac{\epsilon - p}{T^2} = -\frac{N_t}{N_x} a \frac{\partial \log Z}{\partial a} = \frac{N_t}{N_x} \frac{(am)}{\frac{\partial(am)}{\partial \beta}} \left\langle \frac{S}{\beta} \right\rangle. \quad (31)$$

This quantity is also divergent, thus renormalization is needed to obtain a finite value in the continuum, which is achieved simply by using the renormalized action S_{ren} instead of S in the above formula. Below we show the continuum results for different μ/T values as a function of temperature (Fig. 8).

We note, that similarly to inflection point of the pressure, the peak position of the trace anomaly can also serve as a definition of a pseudocritical temperature (T_{pc}) characterizing the transition in the O(3) model.¹

¹ Together with the T_{pc} calculated from the inflection point of the pressure, we show how the pseudocritical temperatures depend on μ/T in Fig. 25.

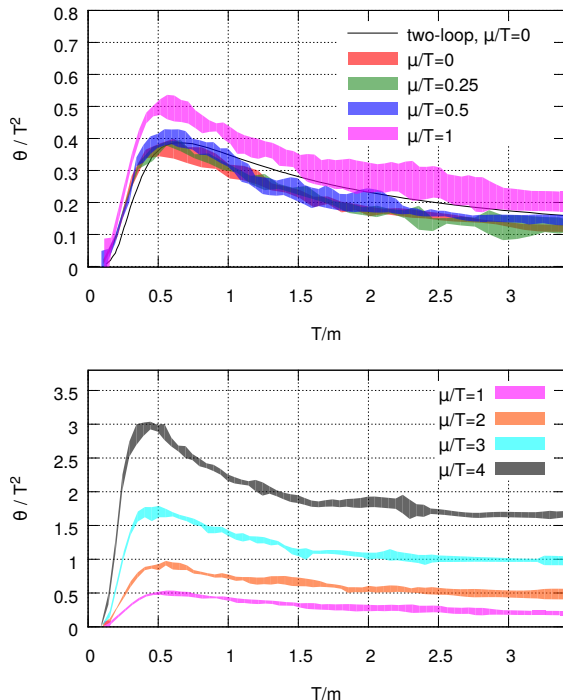


FIG. 8. Continuum results for θ/T^2 as a function of T/m for different μ/T values. The two-loop result for $\mu = 0$ is from [53].

3. Density

Another quantity we measured during the simulations was the density, which is defined through

$$n = \frac{T}{V_{sp}} \frac{\partial \log Z}{\partial \mu} = \frac{T}{V_{sp}} \frac{1}{Z} \frac{\partial Z}{\partial \mu} = \frac{T}{V_{sp}} \left\langle -\frac{\partial S}{\partial \mu} \right\rangle = m \frac{1}{N_t N_x} \frac{1}{am} \left\langle -\frac{\partial S}{\partial (\mu a)} \right\rangle, \quad (32)$$

where V_{sp} is the spatial volume which is simply $N_x a$ in our case. The density does not need to be renormalized, because the divergent part of the action is independent of μ . In the figures we show the dimensionless ratio n/m . With the worm algorithm, the density can be calculated again as a ratio, which has Z in its denominator, and in the numerator there is $\frac{\beta}{2}(e^{\mu a} \times \#_1 - e^{-\mu a} \times \#_2)$, where $\#_1$ is the number of configurations with $v = u + \hat{0}$ and $i_u = -, i_v = +$; $\#_2$ is the number of configurations with $u - \hat{0} = v$ and $i_u = -, i_v = +$. The value of the numerator is constructed the way that is suitable for $\partial S / \partial (\mu a)$ (see the derivative of (22) w.r.t. μa).

As one can observe in Fig. 9, n/m depends almost linearly on T/m . Although we did not perform continuum extrapolation above $T/m \approx 3.5$, the numerical data from 56×14 lattices shows that this linear behaviour also holds at higher temperature, at least up to $T/m \approx 4.6$. The configurations used for the finite density calculation

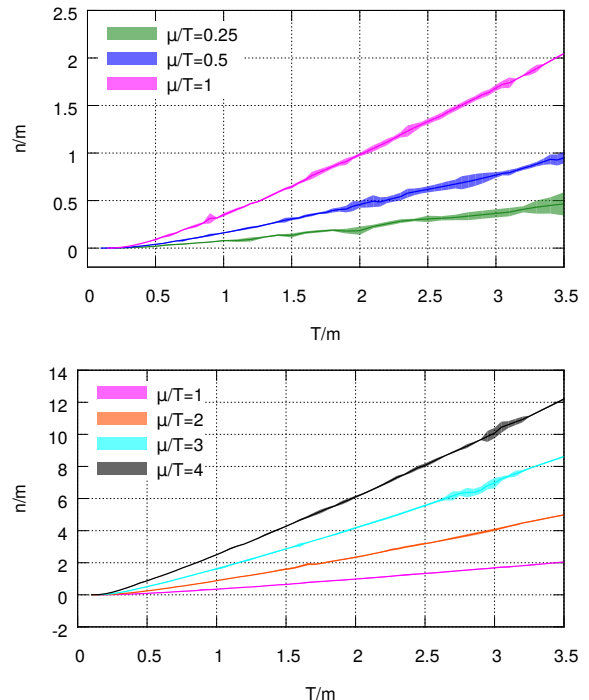


FIG. 9. The density divided by m at finite temperature in the continuum limit.

were the same as for the pressure. We have also analyzed the low temperature behaviour of the density as a function of μ/m , where we observed the well-known Silver Blaze phenomenon (Fig. 10). We approached the $T = 0$ continuum physics by running simulations at fixed β values increasing the volume of the symmetric lattice, then we have extrapolated these $T = 0$ results to the continuum (Fig. 11 and 12). Another way of obtaining the continuum results would be to run simulations at fixed low temperatures and take the continuum limit first, then extrapolate these finite temperature continuum results to $T = 0$. However we did not analyze in full detail this latter case, we performed simulations to obtain the density at two low temperature: $T/m = 0.01$ and $T/m = 0.005$. We compared these to the $T = 0$ results in Fig. 13. For the $T = 0$ results we used $30 \times 30, 60 \times 60, 120 \times 120, 180 \times 180, 240 \times 240, 300 \times 300$ and 360×360 lattices at $\beta = 1, 1.1, 1.2, 1.3, 1.5$, and had runs with $(3.5 \dots 4.5) \times 10^{10}$ steps after thermalization. We also used 500×500 lattices at $\beta = 1.2$ with $(8 \dots 9) \times 10^{10}$ steps and at $\beta = 1.3$ with $(4 \dots 5) \times 10^{10}$ steps, both case after thermalization. The lattices used for the $T/m = 0.01$ results had $N_t = 300, 400, 500, 600$, and spatial volumes $N_x m a = 10, 20, 40, 60, 100$. The spatial volumes $N_x m a = 100$ correspond to symmetric lattices with our choices of β : $\beta = 1.1789$ for $N_t = 300$, $\beta = 1.2644$ for $N_t = 400$, $\beta = 1.3234$ for $N_t = 500$, $\beta = 1.3682$ for $N_t = 600$. For the $T/m = 0.005$ results, we used $N_t = 800, \beta = 1.2644, N_t = 900, \beta = 1.2963, N_t =$

1000, $\beta = 1.3234$, $N_t = 1100$, $\beta = 1.3473$ parameters with spatial volumes $N_x m a = 10, 20, 30, 40, 50, 60, 70$. The number of used worm configurations for these runs were around $(3...7) \times 10^{10}$, after thermalization. Thermalization has taken significantly more steps as one increases the lattice sizes and β . For example in the case of $N_t = 500$, $\beta = 1.3234$ for $N_x m a = 10$ thermalization has taken 3×10^9 , but for $N_x m a = 40$ it was ~ 4.4 times larger, and for $N_x m a = 100$ (symmetric lattice) it was ~ 19 times larger than for $N_x m a = 10$. Thermalization was analyzed using the values of density during the simulations.

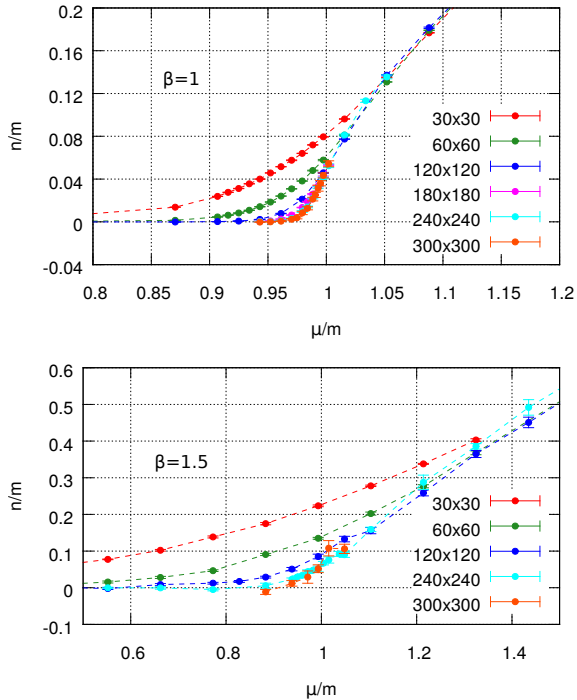


FIG. 10. The density over m at low temperatures at $\beta = 1$ and at $\beta = 1.5$ for different lattice sizes. We used the $T \rightarrow 0$ limit extrapolation based on these results to obtain the continuum limit.

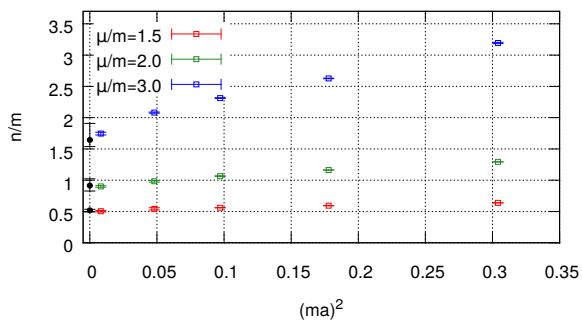


FIG. 11. Continuum extrapolation at some μ/m at $T/m = 0$.

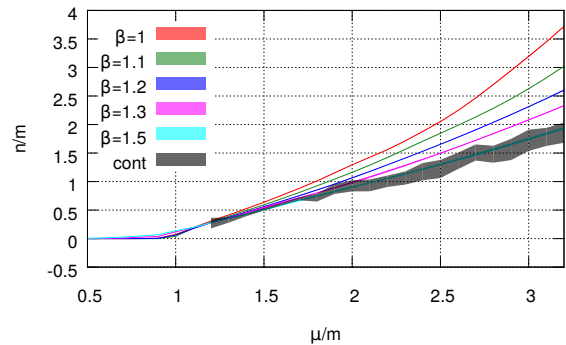


FIG. 12. Continuum limit for n/m at $T/m = 0$ using lattices with fixed β values.

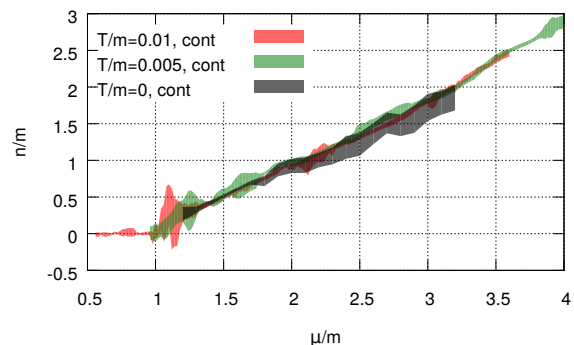


FIG. 13. Comparison of n/m continuum results at $T/m = 0.01, 0.005$ and $T/m = 0$.

VI. THE COMPLEX LANGEVIN ALGORITHM

We proceed with the realisation of the complex Langevin algorithm for the $O(3)$ model. The continuum complex Langevin equation for each component $i = 1, 2, 3$ of a 3-component scalar field variable is

$$\frac{\partial \phi_{x,i}(\tau)}{\partial \tau} = -\frac{\delta S[\phi; \tau]}{\delta \phi_{x,i}(\tau)} + \eta_{x,i}(\tau), \quad (33)$$

where τ is the simulation time, and $\eta_{x,i}(\tau)$ is a Gaussian noise, that obeys the following relations:

$$\langle \eta_{x,i}(\tau) \eta_{x',j}(\tau') \rangle = 2\delta_{ij} \delta_{xx'} \delta(\tau - \tau'), \quad \langle \eta_{x,i}(\tau) \rangle = 0. \quad (34)$$

The simplest discretization for equation (33) is the so called Euler (or Euler-Maruyama) discretization:

$$\phi_{x,i}^{(n+1)} = \phi_{x,i}^{(n)} - \varepsilon \frac{\delta S}{\delta \phi_{x,i}}^{(n)} + \sqrt{\varepsilon} \eta_{x,i}^{(n)}, \quad (35)$$

where we denote the simulation steps with n , and ε is a finite stepsize. However, equation (35) does not preserve the length of the ϕ_x vector, so in order to simulate

the O(3) model we must somehow include the constraint $\sum_i \phi_{x,i}^2 = 1$, because the partition function for the O(3) model is

$$Z = \int \prod_x d\phi_x \delta(\phi_x^2 - 1) e^{-S[\phi]} \\ = \int \prod_x d\phi_x e^{-(S[\phi] - \sum_x \ln \delta(\phi_x^2 - 1))}. \quad (36)$$

Usually the integration measure is not considered explicitly during the integration: one does not use the force arising from the constraint, but uses other (general) coordinates or specific integration. For example suitable general coordinates in our case are spherical coordinates, and an example for a specific integration scheme in Descartes-coordinates is the so called Euler discretization in group space, which is used for example in complex Langevin (CL) simulations of SU(N) gauge groups [26]. In the following we will study these approaches to integrate CL equations.

A. Use of spherical coordinates

In terms of spherical coordinates $\phi_x = (\sin \vartheta_x \cos \varphi_x, \sin \vartheta_x \sin \varphi_x, \cos \vartheta_x)$, and Z becomes

$$Z = \int \prod_{x_1} d\varphi_{x_1} \prod_{x_2} d\vartheta_{x_2} e^{-(S[\varphi, \vartheta] - \sum_x \ln \sin \vartheta_x)} \\ = \int \prod_{x_1} d\varphi_{x_1} \prod_{x_2} d\vartheta_{x_2} e^{-S_{eff}[\varphi, \vartheta]}, \quad (37)$$

where

$$S_{eff}[\varphi, \vartheta] = 2\beta V - \beta \sum_{x, \nu} \left(\sin \vartheta_{x+\hat{\nu}} \sin \vartheta_x \cos(\varphi_{x+\hat{\nu}} - \varphi_x - i\mu a \delta_{\nu,0}) + \cos \vartheta_{x+\hat{\nu}} \cos \vartheta_x \right) - \sum_x \ln \sin \vartheta_x. \quad (38)$$

From this expression one can deduce the drifts:

$$-\frac{\delta S_{eff}}{\delta \varphi_x} = \beta \sum_{\nu} \left(\sin \vartheta_x \left[\sin \vartheta_{x+\hat{\nu}} \sin(\varphi_{x+\hat{\nu}} - \varphi_x - i\mu a \delta_{\nu,0}) - \sin \vartheta_{x-\hat{\nu}} \sin(\varphi_x - \varphi_{x-\hat{\nu}} - i\mu a \delta_{\nu,0}) \right] \right), \quad (39)$$

and

$$-\frac{\delta S_{eff}}{\delta \vartheta_x} = \beta \sum_{\nu} \left(\cos \vartheta_x \left[\sin \vartheta_{x+\hat{\nu}} \cos(\varphi_{x+\hat{\nu}} - \varphi_x - i\mu a \delta_{\nu,0}) + \sin \vartheta_{x-\hat{\nu}} \cos(\varphi_x - \varphi_{x-\hat{\nu}} - i\mu a \delta_{\nu,0}) \right] - \sin \vartheta_x (\cos \vartheta_{x+\hat{\nu}} + \cos \vartheta_{x-\hat{\nu}}) \right) - \frac{1}{\tan \vartheta_x}. \quad (40)$$

Then the discretized complex Langevin steps are

$$\varphi_x(n+1) = \varphi_x(n) + \varepsilon_n K_x^{(\varphi)}(n) + \sqrt{\varepsilon_n} \eta_x^{(\varphi)}(n), \quad (41)$$

$$\vartheta_x(n+1) = \vartheta_x(n) + \varepsilon_n K_x^{(\vartheta)}(n) + \sqrt{\varepsilon_n} \eta_x^{(\vartheta)}(n), \quad (42)$$

where $K_x^{(\varphi)} = -\delta S_{eff} / \delta \varphi_x$ and $K_x^{(\vartheta)} = -\delta S_{eff} / \delta \vartheta_x$. In these equations $\eta_x^{(\varphi)}$ and $\eta_x^{(\vartheta)}$ are real, Gaussian noises, and the finite stepsize ε_n is determined adaptively, so also depends on n . As one can observe, the force $-\delta S_{eff}[\varphi, \vartheta] / \delta \vartheta_x$ is singular because of the $1/\tan \vartheta_x$ term. In order to avoid overflow during the simulations due to the singular forces, one can do constraint simulation and truncate the configuration space to avoid the values of ϑ_x near 0 and π . If the stepsize is not small enough it is needed in order to get stable simulation runs. We achieved this by reflecting the trajectories in the following way:

$$\vartheta_x(n+1) := \begin{cases} 2\vartheta_{\text{LIM}} - \vartheta_x(n+1), & \text{if } \vartheta_x(n+1) < \vartheta_{\text{LIM}}, \\ \vartheta_x(n+1), & \text{if } \vartheta_{\text{LIM}} < \vartheta_x(n+1) < \pi - \vartheta_{\text{LIM}}, \\ 2(\pi - \vartheta_{\text{LIM}}) - \vartheta_x(n+1), & \text{if } \pi - \vartheta_{\text{LIM}} < \vartheta_x(n+1). \end{cases} \quad (43)$$

The border value for ϑ was defined with a parameter ϑ_{LIM} . Results shown later suggests the somewhat natural expectation that if ε and ϑ_{LIM} are small enough, then the results are independent of their values.

B. Integration in group space

Using ideas from CL equation on SU(N) gauge groups [26], one can write a specific integration scheme that uses Descartes-coordinates, but takes the constraint into account: the Euler discretization (which we call now the exponentialized Euler-Maruyama discretization). For the O(3) group elements O_x , this is the following

$$O_x(n+1) = R_x(\varepsilon) O_x(n). \quad (44)$$

Since all ϕ_x can be written with some ϕ_0 constant unit vector and with an O_x rotation matrix as $\phi_x = O_x \phi_0$, the above time evolution can turn into the time evolution of the original ϕ_x variables.

The $R_x(\varepsilon)$ in Formula (44) can be written in different ways. It can be e.g.

$$R_x^{(1)}(\varepsilon) = \exp \left(\sum_a t_a (\varepsilon K_{ax} + \sqrt{\varepsilon} \eta_{ax}) \right), \quad (45)$$

or

$$R_x^{(2)}(\varepsilon) = \prod_{a \in (1,2,3)} \exp(t_a (\varepsilon K_{ax} + \sqrt{\varepsilon} \eta_{ax})), \quad (46)$$

or

$$R_x^{(3)}(\varepsilon) = \prod_{a \in (1,2,3)} \exp(t_a \varepsilon K_{ax}) \exp(t_a \sqrt{\varepsilon} \eta_{ax}). \quad (47)$$

Since $e^{A+B} \neq e^A e^B$, when $[A, B] \neq 0$, these are not equivalent to each other at finite ε , but the difference is not detectable at the numerical precision and parameter set we used. Due to this, during our simulations we used $R_x^{(2)}$, which is not the computationally cheapest version (it is $R_x^{(1)}(\varepsilon)$), but the cheapest version that evolves the system in each direction in the tangent space individually one after another. In the expressions above, the t_a s are the 3 generators of $O(3)$ in the 3-dimensional representation. The drift K_{ax} is

$$\begin{aligned} K_{ax} &= -D_{ax}S[O] = -\partial_\alpha S[e^{\alpha t_a} O_x]|_{\alpha=0} \\ &= \beta(\phi_0^T O_{x+\hat{0}}^T e^{i\mu at_3} t_a O_x \phi_0 - \phi_0^T O_x^T t_a e^{i\mu at_3} O_{x-\hat{0}} \phi_0 \\ &\quad + \phi_0^T O_{x+\hat{1}}^T t_a O_x \phi_0 - \phi_0^T O_x^T t_a O_{x-\hat{1}} \phi_0) \\ &= \beta(\phi_{x+\hat{0}}^T e^{i\mu at_3} t_a \phi_x - \phi_x^T t_a e^{i\mu at_3} \phi_{x-\hat{0}} \\ &\quad + \phi_{x+\hat{1}}^T t_a \phi_x - \phi_x^T t_a \phi_{x-\hat{1}}). \end{aligned} \quad (48)$$

With ϕ^T and O^T we denote the transpose of ϕ and O , and η_{ax} is the usual Gaussian noise. The time evolution determined by Eq. (44) then can be written with ϕ_x as

$$\phi_x^{(n+1)} = \prod_{a \in (1,2,3)} \exp[(\varepsilon_n K_{ax} + \sqrt{\varepsilon_n} \eta_{ax}) t_a] \phi_x^{(n)}. \quad (49)$$

In particular we performed the updates by varying the order of the 3 matrix multiplication randomly. Higher order integrations, like Runge-Kutta [51] are also possible:

$$\begin{aligned} \phi'_x &= \exp\left[(\varepsilon_n K_{ax}[\phi^{(n)}] + \sqrt{\varepsilon_n} \eta_{ax}) t_a\right] \phi_x^{(n)} \\ \phi_x^{(n+1)} &= \exp\left[\frac{\varepsilon_n}{2} \left(1 + \frac{C_A \varepsilon_n}{6}\right) (K_{ax}[\phi^{(n)}] + K_{ax}[\phi']) t_a\right. \\ &\quad \left. + \sqrt{\varepsilon_n} \eta_{ax} t_a\right] \phi_x^{(n)}, \end{aligned} \quad (50)$$

where $C_A = 2$ is the Casimir invariant for the three-dimensional representation of $O(3)$.

C. Direct method to include the constraint in Descartes-coordinates

Using Descartes coordinates, the constraining force can be considered by using a term arising from $-\sum_x \ln \delta(\phi_x^2 - 1)$, see eq. (36). This is also singular, so one can attempt to approximate the Dirac-delta with a sharp Gaussian, $(\sqrt{2\pi b})^{-1} e^{-x^2/(2b^2)} \rightarrow \delta(x)$, as $b \rightarrow 0$. The force is then

$$\begin{aligned} K_x &= -\frac{\delta}{\delta \phi_x} \left(S[\phi] - \sum_y \ln \delta(\phi_y^2 - 1) \right) \\ &= \beta (\phi_{x+\hat{0}} e^{i\mu at_3} + e^{i\mu at_3} \phi_{x-\hat{0}} + \phi_{x+\hat{1}} + \phi_{x-\hat{1}}) \\ &\quad - \frac{2}{b^2} (\phi_x^2 - 1) \phi_x, \end{aligned} \quad (51)$$

where the last term helps to keep the length of ϕ_x near 1. Then fields evolve according to

$$\phi_{x,i}^{(n+1)} = \phi_{x,i}^{(n)} + \varepsilon_n K_{x,i}^{(n)} + \sqrt{\varepsilon_n} \eta_{x,i}^{(n)}, \quad (52)$$

where again ε_n is the finite stepsize determined adaptively, and the noise is Gaussian with $\sqrt{2}$ width. Note that using this time evolution, the $\sum_i \phi_{x,i} = 1$ condition is no longer true during the simulations, but the force can push the field into this direction. We refer to this time evolution as 'standard Euler-Maruyama discretization with Dirac-delta' in the following.

In the next Section we discuss the results obtained using the algorithms under review.

VII. COMPARISON OF RESULTS

As was discussed in the Introduction, the complex Langevin algorithm may provide a relatively easily feasible way to study sign problems in different models, but may converge to wrong results, which lowers the reliability of the simulation when there are no alternative results in the problematic parameter range. The conventional reasoning of explaining the wrong results is that the justification of complex Langevin [23–25] is not correct in that parameter range, because some observables develop long tailed distributions. (For details we refer to [24].) However, in some models (e.g. in a random-matrix model [54, 55]) it was observed that using different variables in describing the model can help to eliminate this problem. This can imply that the failure of the algorithm is not because physics has changed, but because of some unknown algorithmic details. The source of these can be quite broad. One can think of systematic errors originating from e.g. stepsize to zero limit, low randomness in the random number generator, floating point roundoff errors, or not taking the continuum limit etc., or sampling errors because low autocorrelation for example due to some distinguished region in configuration space, etc. In the following we analyse some of these aspects in the case of the 1+1 dimensional $O(3)$ model. The results are compared to the worm results, which are referred to as the correct ones in the text.

Although we used adaptive stepsize in all our simulations, this can not replace the completion of the $\varepsilon \rightarrow 0$ extrapolation of the results. (Of course its effect depends on the used numerical precision and the algorithm under study as well as other subtle circumstances. For example, as we will see the simulations with spherical coordinates do not depend in a detectable way on ε at the simulations with the used set of parameters for e.g. the action variable.) In the following, first, we discuss the results for the action S and the trace anomaly θ , then for the density n/m .

A. Action and trace anomaly

Using **spherical coordinates** to parametrize the model, we had run simulations at 56×14 lattices, at $\mu a = 0, 0.018, 0.071, 0.143, 0.2143, 0.286$, that is at $\mu/T = 0, 0.25, 1, 2, 3, 4$. We had some exploratory runs at $\mu a = 0, 0.018, 0.2143$ using $\varepsilon = 0.0005, 0.0002$ and only $\vartheta_{\text{LIM}} = 10^{-5}$, and at $\mu a = 0.286$ using $\varepsilon = 0.0005, 0.0001$ and $\vartheta_{\text{LIM}} = 10^{-5}, 10^{-8}$. At $\mu a = 0.071, 0.143$ we had $\varepsilon = 0.001, 0.0001$ also. Although we found that there is no detectable stepsize dependency of the results, we extrapolate to zero stepsize at $\mu a = 0.071$ and 0.143 using four stepsizes. We also find that the results do not depend on ϑ_{LIM} if it is chosen quite small by testing this question at $\mu a = 0.071$ using $\vartheta_{\text{LIM}} = 10^{-3}, 10^{-5}, 10^{-7}, 10^{-8}, 10^{-11}$ simulations with $\varepsilon = 0.0005$. We also run simulations on 72×18 lattices at $\mu/T = 1$, with $\varepsilon = 0.0001, \vartheta_{\text{LIM}} = 10^{-5}$. In all these simulations β was set between 0.95 and 1.8 , and $1000 \dots 1600$ Langevin trajectories were used.

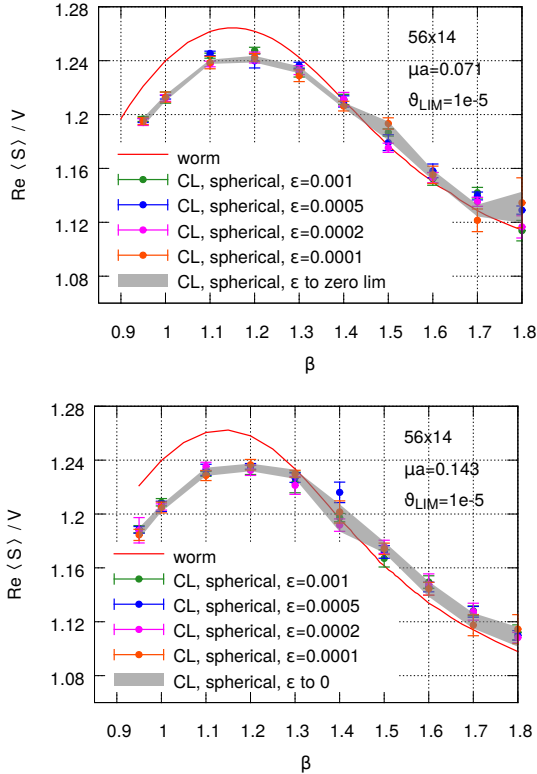


FIG. 14. CL results for $\text{Re}\langle S \rangle / V$ with spherical coordinates. Top: $\mu a = 0.071$ ($\mu/T = 1$), bottom: $\mu a = 0.143$ ($\mu/T = 2$).

We found that at $\mu a = 0$ spherical CL results agree completely with the correct results. At $56 \times 14, \mu a = 0.018$ they deviate below $\beta \sim 1.3$. This clearly shows that the wrong convergence property is not the consequence of the severeness of the sign problem, because it is very mild at $\mu a = 0.018$ (see Fig. 2, right panel). We note, that CL results obtained with spherical coordinates seem to slightly deviate from the correct ones in the high

β region as well, but these differences are not significant statistically (they are within 2 sigma). At high μ/T however the deviations are significant, so at e.g. $\mu a = 0.286, 56 \times 14$, results for the action are wrong at all β values. Since this discretization is a bit problematic due to the singularity in the force, and deviations at high μ/T seemed discouraging, we do not tested so carefully its continuum behaviour or possible improvements. However, we mention that using 72×18 lattices did not show any improvement at $\mu/T = 1$. We show some of the results in Fig. 14.

We have investigated the **group integration approach** (Subsection VI B) more carefully. First, we compared simulation results of using $R^{(1)}, R^{(2)}$ or $R^{(3)}$ at 56×14 lattices at $\mu a = 0.071, \varepsilon = 0.0005$ using 2000 Langevin trajectories at several β in the range $0.9 \dots 1.8$. We found complete agreement using these parameters. Then we used $R^{(2)}$ during our further simulations with the exponentialized Euler-Maruyama discretization (abbreviated in the following and in the Figures as *exp. E-M*). We carried out simulations on 32×8 lattices at $\mu/T = 0.25$, on $40 \times 10, 56 \times 14, 64 \times 16, 72 \times 18, 80 \times 20$ lattices at $\mu/T = 0, 0.25, 0.5, 1, 2, 3, 4$ in the β range $0.9 \dots 1.8$ and on 120×30 and 200×50 lattices at $\mu/T = 0.5, 3.0$.

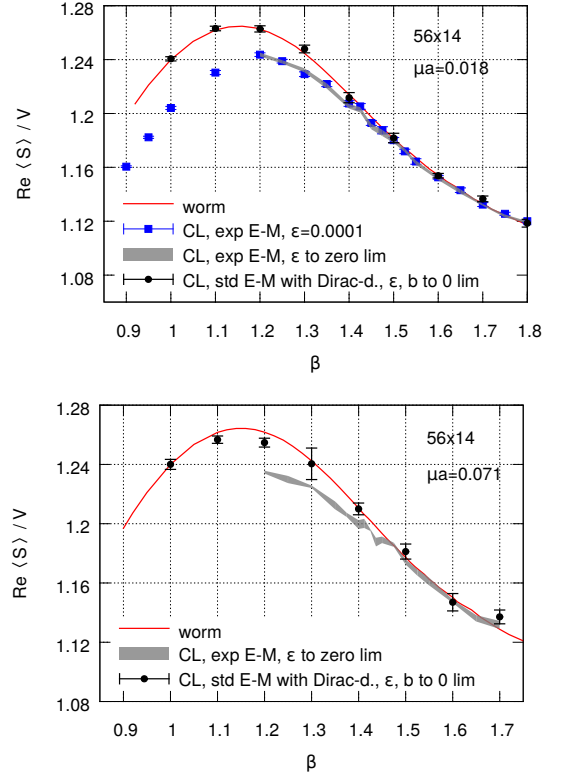


FIG. 15. The comparison of $\text{Re}\langle S \rangle / V$ results for different algorithms: worm, CL with exponentialized E-M, CL with standard E-M discretization with Dirac- δ . Top: $\mu a = 0.018$ ($\mu/T = 0.25$), bottom: $\mu a = 0.071$ ($\mu/T = 1$). Note that the exp. E-M method is wrong at low β even when the sign problem is very mild.

Several initial stepsizes were used during these simulations: $\varepsilon = (10, 5, 2, 1) \times 10^{-4}$ and in many cases $\varepsilon = (8, 5, 2, 1) \times 10^{-5}$. We extrapolated these into the stepsize to zero limit. (However, we note, that we did not find significant stepsize dependency of the results obtained with stepsizes 10^{-4} and smaller.) The Langevin trajectories were between 3800 and 5500 after thermalization at most β , at some there were fewer trajectories (but more than 1200), and at some β we also tested very long runs, that is 10^4 Langevin trajectories.

We came into similar conclusions as with spherical coordinates: at $\mu/T = 0$ complete agreement was found, then at μ/T nonzero – even at $\mu/T = 0.25$ –, a discrepancy in the low β region. We note however, that the exp. E-M. results do not deviate from the correct results at higher β values. In order to quantify the deviations and investigate their continuum behaviour, we first calculated $(\langle S_w \rangle - \text{Re}\langle S_{cl} \rangle)/V/\sigma$, where $\langle S_w \rangle$ is the worm result, $\langle S_{cl} \rangle$ is the exp. E-M result in the $\varepsilon \rightarrow 0$ limit, $V = N_x \times N_t$ is the lattice volume and $\sigma = \sqrt{\Delta_w^2 + \Delta_{cl}^2}$, where Δ_w , Δ_{cl} are the full errors of the worm and CL simulations, respectively. (Δ_w is just the statistical error, but Δ_{cl} contains systematic errors because of the stepsize extrapolation.) After that, we determined a β region at each lattice size and μa parameter, when $(\langle S_w \rangle - \text{Re}\langle S_{cl} \rangle)/V/\sigma$ started to be above 2. This definition of the β range (the latest point under 2 sigma, and two successive points above 2 sigma) is a bit ambiguous in the sense that it depends on the statistics, but we did not find significant differences between the results of some smaller statistics run and the long runs. Figure 16 shows an example of the determination of this β range. Then the middle of this range with errors to cover the whole range were used to calculate $T_{threshold}^{(S(\beta))}/m$, the temperature below which CL converges to wrong results at the lattice under study. We show how these temperatures depend on the temporal lattice size at $\mu/T = 3$ in Figure 17. In that Figure one can see that these threshold temperatures become lower as N_t increases, but we do not know the scaling of this quantity as a function of the lattice spacing or N_t , thus we can not extrapolate to the continuum without assumptions. In order to avoid these assumptions, we have calculated the continuum limit of $(\langle S_w(T, \mu/T) \rangle - \text{Re}\langle S_{cl}(T, \mu/T) \rangle)/V$ and then determined the *continuum* threshold temperature $T_{threshold}^{(S)}/m$ below which the continuum results deviate from zero. The results for these temperatures (with further relevant temperature ranges discussed in the text) are shown in Figure 25.

Of course, one can discuss the deviations of the correct and the CL action density in terms of a more standard physical quantity which has a continuum limit: the trace anomaly. So we have also used the trace anomaly and investigated what happens with the continuum limit of the ‘wrong’ complex Langevin results (Fig. 19), and obtained similar threshold temperature values.

We have also made some runs to test this approach against a change in computer numerical precision and the

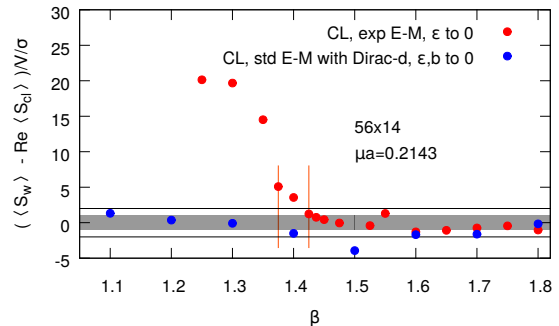


FIG. 16. $(\langle S_w \rangle - \text{Re}\langle S_{cl} \rangle)/V/\sigma$ at $\mu a = 0.143$ ($\mu/T = 2$) (top) and at $\mu a = 0.2143$ ($\mu/T = 3$) (bottom). The grey band shows the 1 sigma, and the black lines the 2 sigma interval. The orange lines show the beta threshold range, below which exp. E-M complex Langevin fails.

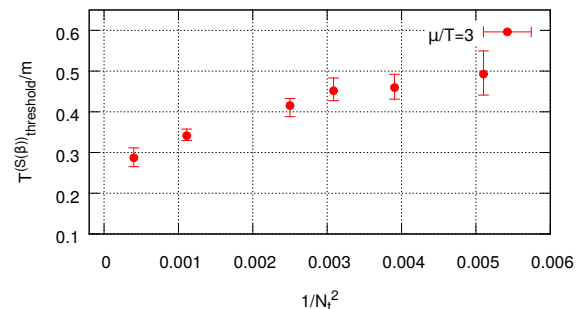


FIG. 17. The temperature $T_{threshold}^{(S(\beta))}/m$ as a function of $1/N_t^2$ at $\mu/T = 3$. Below $T_{threshold}^{(S(\beta))}/m$ the action densities obtained by the exp. E-M discretization start to become wrong. The figure shows that using larger lattices this temperature becomes lower, but the continuum extrapolation of this quantity can not be made without assuming some functional dependence of it as a function of $1/N_t$, which would hinder to draw the conclusion.

order of integration. That is we used float and long double precision, and found that although float and double differ from each other (float is wrong at all β), double and long double are almost the same at the parameters used to clarify this (56×14 , $\mu/T = 0.071, 0.143$, $\varepsilon = 0.0005$, ~ 1800 Langevin traj.). We have also tested exponentialized Runge-Kutta integration at double precision, but results did not improve.

We have also checked the shape of the distributions, and these are shown in Fig. 18. One can see that the distributions are narrower in the high temperature range.

Finally, let us discuss the results obtained using the **standard Euler-Maruyama discretization** with a Dirac-delta approximated with a Gaussian. We simulated with this algorithm at 40×10 , 56×14 , 64×16 , 72×18 and 80×20 lattices at $\mu/T = 0, 0.25, 1, 2, 3, 4$. We used several initial stepsizes ($\varepsilon = (5, 2, 1) \times 10^{-4}$, $\varepsilon = 5 \times 10^{-5}$ and in some cases $\varepsilon = (8, 2) \times 10^{-5}$), and at

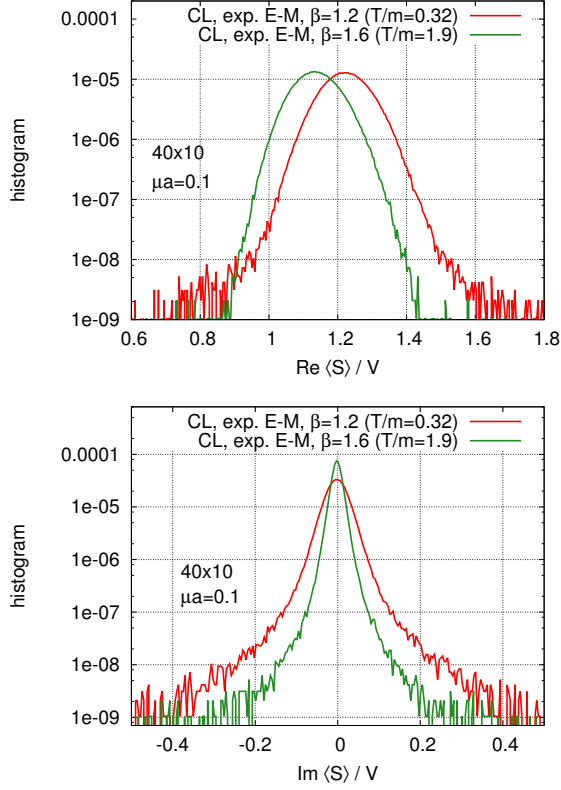


FIG. 18. The histogram of $\text{Re}\langle S \rangle / V$ (top) and $\text{Im}\langle S \rangle / V$ (bottom) at $\beta = 1.2$ and $\beta = 1.6$. These β values correspond to $T/m = 0.32$ and $T/m = 1.9$, the former is such a temperature where the complex Langevin exp. E-M discretization develops wrong results for the action, the latter is a temperature where it is correct. One can see that the histograms indeed show the usual concomitant sign of wrong results, that is the longer tail of the distribution of the observables.

each stepsize we used several b value ($0.01 < b < 0.06$). Using double precision, we found that at a given stepsize, below a low b value, simulations became unstable, so there we used long double precision to set lower b values. At each stepsize we extrapolated to $b \rightarrow 0$, then used these results to extrapolate in ε . At most β the used Langevin trajectories were between 2000 and 3000. When we introduced this method in Subsection VIC, we mentioned that this algorithm does not keep the $\sum_i \phi_i^2 = 1$ constrain rigorously during the simulation. To characterize it quantitatively, we measured the length of the ϕ vectors over the lattice and found it is typically a bit larger than 1, but with smaller b and ε values it can be reduced (see the lower panel of Fig. 20). We found that after taking both the b to zero (Fig. 20, top), and ε to zero limit, the results obtained by this method agree well with the correct results (Fig. 15, Fig. 16). These results are interesting because when we accomplish the b to zero and ε to zero limits, the used datas may have distributions also with some non-exponential decay, see Figure 21. The obtained histograms were compared to those of the exp. E-M discretization and one can see that

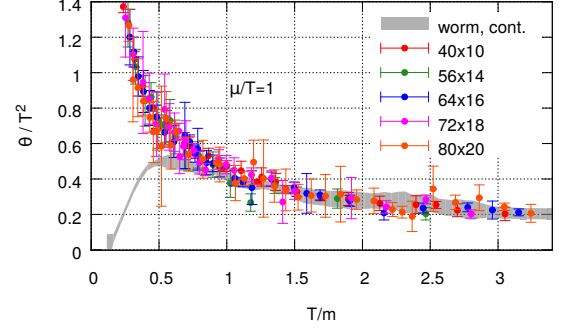


FIG. 19. The trace anomaly determined with the complex Langevin algorithm using the exp. E-M discretization and the worm algorithm. Although we do not plot the continuum limit of the complex Langevin results here, the results suggest that there is no improvement towards the continuum.

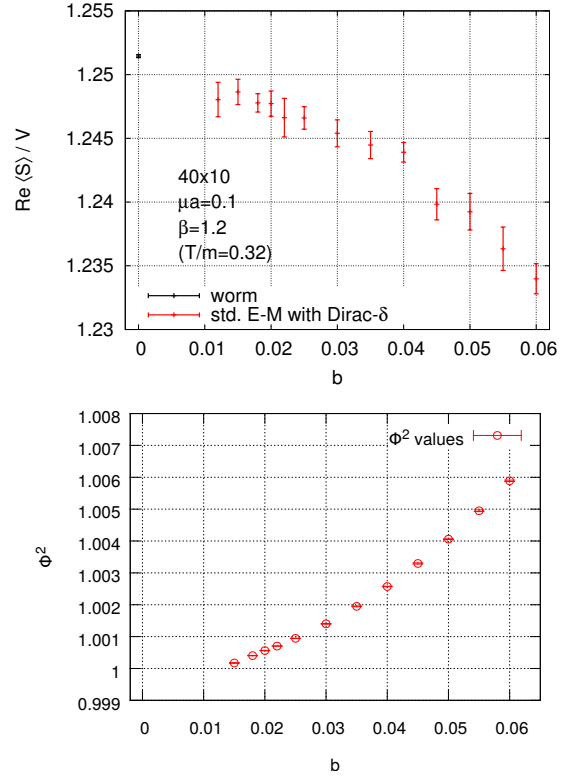


FIG. 20. Top: The Figure shows how taking the $b \rightarrow 0$ limit can help to obtain the correct results for the action with the standard E-M implementation (the starting ε stepsize was $5 \cdot 10^{-5}$ during the simulations to obtain the datapoints of the figure). Bottom: The effect of the reduction of the b parameter on the average length of ϕ vectors.

the decay of the standard E-M discr. with Dirac- δ seems to be sharper (Fig. 21). For completeness, we mention here that the errors coming from the two extrapolations become significantly larger, especially at small β s as the chemical potential increases.

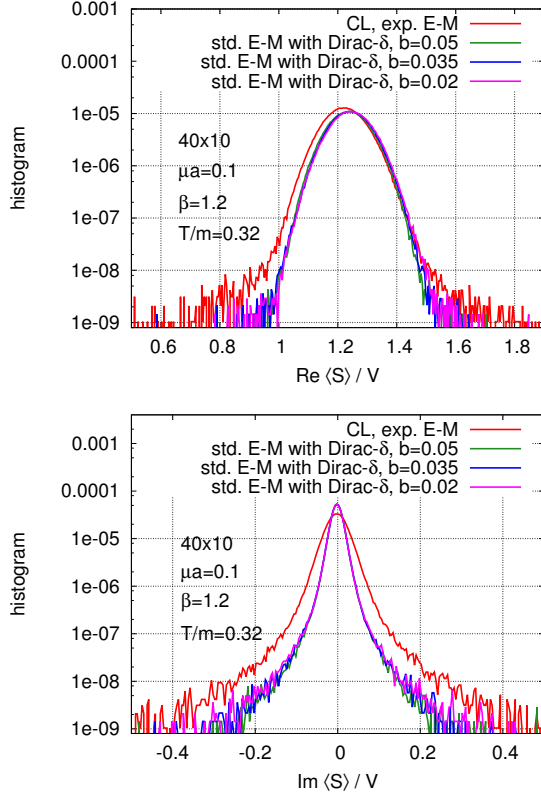


FIG. 21. Histograms of $\text{Re}(S)/V$ (top) and $\text{Im}(S)/V$ (bottom) at $\beta = 1.2$ obtained with the exp. E-M implementation and with the std. E-M implementation with Dirac- δ . We see, that the std. E-M implementation develops quite similar distributions for the real part of the action, while narrower for the imaginary part. The shape of the histograms do not change so much as decreasing b (the width of the Gaussian, that approximates the Dirac- δ), although results get closer to the correct ones.

B. Density

In the present Subsection, we review the results for the density (Eq. (32)) obtained by the different algorithms. For the worm results and complex Langevin implementations, we used the same configurations as listed in the above Subsections. For reweighting results we used the cluster algorithm to simulate at $\mu = 0$ and used 3×10^6 updating steps.

We found that reweighting results agree well with the worm results below $\mu a \sim 0.16$ on 56×14 lattices, that is below $\mu/T \sim 2.2$ (see Figure 22). At higher μa values the results have large errorbars and deviations from correct results occurs. This coincides with the fact that the sign problem becomes severe at these lattices around $\mu a \sim 0.15$ (Fig 4).

Regarding the different CL implementations we found that both the exp. E-M integration and the standard E-M with Dirac- δ produces wrong results at low temperature (Fig. 22).

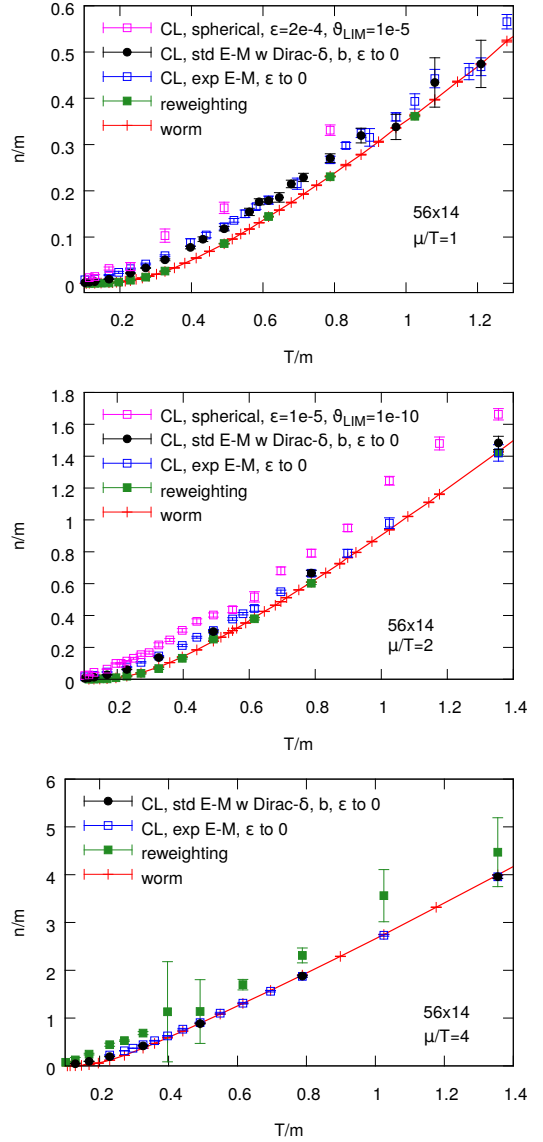


FIG. 22. The density at low temperature measured on 56×14 lattices, at $\mu/T = 1$ (top), at $\mu/T = 2$ (middle) and at $\mu/T = 4$ (bottom). At $\mu/T = 4$ the reweighting results become unreliable, while CL remains correct if the temperature is greater than $0.37 \dots 0.5$.

A threshold temperature ($T_{\text{threshold}}^{(n/m)}/m$) can be defined similarly as we did in the case of the action: this is the temperature below which continuum CL density results deviate from the continuum worm density results with 2 sigma significance. A comparison of the continuum results from the exp. E-M. CL and the worm algorithm can be seen in Fig. 23. We note that in the low temperature region, the continuum extrapolation takes the CL results even further from the worm continuum results. By increasing the chemical potential one can observe that $T_{\text{threshold}}^{(n/m)}/m$ is approximately constant, then gets smaller (see Fig. 24 and 25). We note, that the

$T_{threshold}^{(n/m)}$ values are approximately the same for the exp. E-M. discretization and for the standard E-M. discretization with Dirac- δ .

The spherical CL implementation also develops wrong results, but its threshold temperature seems to be larger than that of the others. However, we note that in the case of the spherical formulation we did not determined so carefully the threshold temperature.

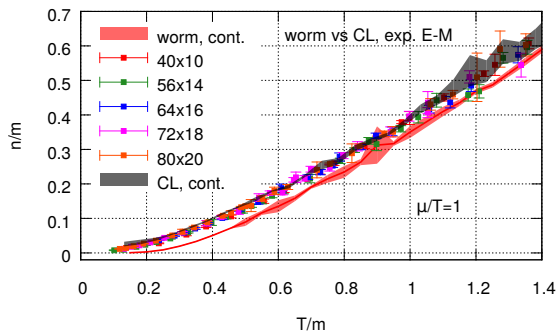


FIG. 23. Comparison of the continuum results for the density obtained by the worm and the CL, exp. E-M discretization at $\mu/T = 1$. The figure shows that the continuum extrapolation from the complex Langevin results differs from the worm continuum result.

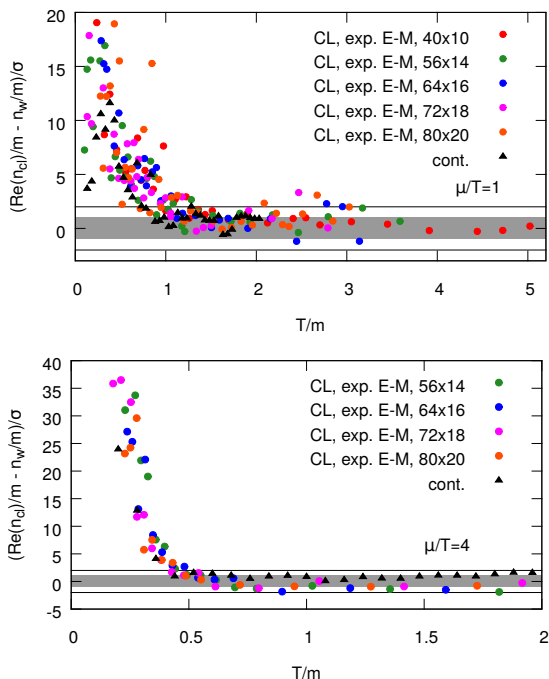


FIG. 24. The density differences of different complex Langevin results (n_{cl}/m) and the worm (n_w/m) divided by $\sigma = \sqrt{\Delta_{cl}^2 + \Delta_w^2}$ at $\mu/T = 1$ (top) and at $\mu/T = 4$ (bottom). The figure shows that the threshold temperature does not reduce toward the continuum. The black triangles are calculated from the continuum CL density and the continuum worm density.

The distributions of the real and imaginary part of

$\partial S/\partial(\mu a)$ are again narrower, when different complex Langevin algorithms produce correct results. Comparing the distributions for this quantity of the exp. E-M and std. E-M with Dirac- δ implementations we see that although the latter is narrower, the results do not converge to the correct results as in the case of the action they did.

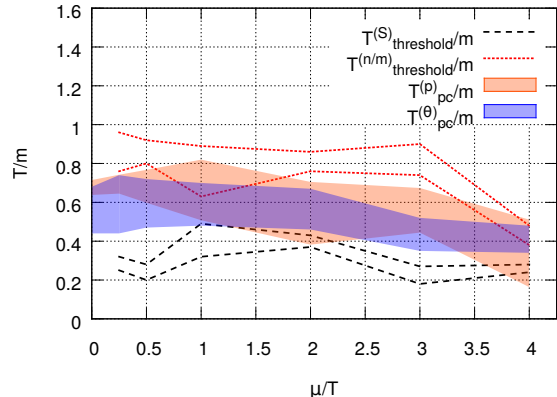


FIG. 25. The figure shows the temperatures $T_{threshold}/m$ determined from the action differences and the density differences discussed in the text. Below $T_{threshold}^{(S)}/m$, the exp. E-M discretization develops wrong results for the action. The std. E-M discretization with Dirac- δ produces correct results for the action at all temperature. However, both implementations give wrong results for the density below $T_{threshold}^{(n/m)}$. The blue and red solid bands show the pseudocritical temperatures determined from inflection point of the pressure and from the maximum of the trace anomaly, $T_{pc}^{(p)}/m$ and $T_{pc}^{(\theta)}/m$, respectively.

VIII. CONCLUSION

In the present paper we studied the sign problem in the O(3) model. We used reweighting in order to investigate the severeness of the sign and overlap problem. We described a dual formalism and based on that a worm algorithm, which completely solves the sign problem. Using this, we have calculated the pressure, the trace anomaly and the density at finite temperature. At zero and low temperature we reproduced the Silver Blaze phenomenon. We then analysed the correctness of the complex Langevin as approaching the continuum limit. The failure of complex Langevin in certain parameter ranges is argued to be the consequence of the developing long tailed distributions. However it is an interesting question whether the wrong convergence property happens at a specific β value – as was found in HDQCD [29] – or at a given temperature. In the former case continuum extrapolation could enable one to study the full phase diagram of the given model. According to recent results [7] the breakdown seems to prevent the exploration of the

confined region in QCD, however simulations used only $N_t = 4, 6, 8$ lattices. In the present paper our main goal was to investigate whether taking the continuum limit in the 1+1 dimensional O(3) model can help to overcome the wrong convergence property of complex Langevin.

For this purpose we have used three different approach: describing the model with spherical coordinates; using the generators and integrate the CL equations in the group space (exp. Euler-Maruyama); and considering the $\sum_i \phi_i^2 = 1$ constrain with a term containing the logarithm of a Dirac- δ in the action (standard Euler-Maruyama discr. with Dirac- δ). We approximated the Dirac- δ with a Gaussian with width $\sim 1/b$. We analysed three observables: the action, the trace anomaly and the density. Regarding the action, we found that both the spherical coordinates and the exp. Euler-Maruyama discretization give wrong results at the low β (low temperature) range. For the exp. Euler-Maruyama discretization, we analysed whether taking the continuum limit can help to improve the results and found that although the accessible temperature range becomes larger, one cannot explore the full low temperature region. However, we established that the so called standard Euler-Maruyama discr. with Dirac- δ method can give correct results for the action density after taking both the b to zero and ε to zero limits. We found that for the density observable the situation is different: here this latter way of integrating CL equations gives also wrong results at low T/m and results seem to not improve by taking larger and finer lattices.

IX. ACKNOWLEDGEMENTS

The authors thank Dénes Sexty for discussions and useful comments on the manuscript. The work was supported by the Lendület program of the HAS (LP2012-44/2012) and by the OTKA-NF-104034 grant from OTKA.

Appendix A: Appendix

In this Appendix, we describe our updating steps of the worm algorithm in detail. As in the beginning of Sec. V (before VD), we consider the general case $O(N)$ in $d + 1$ dimensions.

1. Updating steps of the worm algorithm

When μ is zero, we consider three simple updating steps.

1. Move the head of the worm from the position u along a link l to the new position u' . To keep the constraints, by this we increase or decrease the corresponding link variable $m = m_i^{(l)}$ by one. (Here i is the index of

the worm.) The corresponding $2d$ possibilities are chosen with equal probabilities.

1a. Propose to increase the link variable, $m' = m + 1$. The corresponding acceptance probability is $p_{acc} = \min\{q, 1\}$, where

$$q = \frac{\beta k_i(u') + 1}{m' k(u') + N}. \quad (\text{A1})$$

1b. Propose to decrease the link variable, $m' = m - 1$. When $m = 0$ then the move is rejected, otherwise the corresponding acceptance probability is given by

$$q = \frac{m (k'(u) + N)}{\beta (k_i(u) + 1)}. \quad (\text{A2})$$

2. When the two heads of the worm coincide, the worm can jump to a new position, and change its index ($u = v \rightarrow u' = v', i \rightarrow j$). In this case

$$q = \frac{(k(u) + N - 2)(k_j(u') + 1)}{(k_i(u) - 1)(k(u') + N)} = \frac{(\hat{k}(u) + N)(\hat{k}_j(u') + 1)}{(\hat{k}_i(u) + 1)(\hat{k}(u') + N)} \quad (\text{A3})$$

3. Propose to increase or decrease a link variable $m \equiv m_j^{(l)}$ by 2, without changing the worm variables u, v, i .

3a. Propose to increase: $m \rightarrow m' = m + 2$. The acceptance probability is given by

$$q = \frac{\beta^2}{m'(m' - 1)} \prod_{x \in \partial l} \frac{k_j(x) + 1}{k(x) + N}, \quad (\text{A4})$$

3b. Propose to decrease: $m \rightarrow m' = m - 2$. When $m < 2$ the proposal is rejected, otherwise the acceptance probability is given by

$$q = \frac{m(m - 1)}{\beta^2} \prod_{x \in \partial l} \frac{k'(x) + N}{k'_j(x) + 1}. \quad (\text{A5})$$

2. Worm update with chemical potential

According to the representation, Eq. (21) of the scalar product, the index of head and tail of the worm could be $(i_u, i_v) = (-, +), (3, 3), \dots, (N, N)$, hence we have to distinguish two types of the worm. For the type $(i_u, i_v) = (j, j)$ the updating steps described in A 1 remain unchanged. The same is true for updating a link variable $m_j^{(l)}$ for $j = 3, \dots, N$. Below we consider the case $(i_u, i_v) = (-, +)$.

1. Moving the $(-)$ end of the worm in direction $+\hat{\nu}$ from u to $u' = u + \hat{\nu}$

1a. Propose to increase the variable $m_+ \rightarrow m'_+ = m_+ + 1$ on the corresponding link:

$$q = e^{\mu\nu} \frac{\beta k_{12}(u') + 1}{m'_+ k(u') + N} \quad (\text{A6})$$

1b. Propose to decrease the link variable $m_- \rightarrow m'_- = m_- - 1$: if $m_- = 0$, then the proposal is rejected, otherwise

$$q = e^{\mu\nu} \frac{m_- k'(u) + N}{\beta k'_{12}(u) + 1}. \quad (\text{A7})$$

2. Moving the $(-)$ end of the worm in direction $-\hat{\nu}$ from u to $u' = u - \hat{\nu}$:

2a. Propose to increase the link variable $m_- \rightarrow m'_- = m_- + 1$:

$$q = e^{-\mu\nu} \frac{\beta k_{12}(u') + 1}{m'_- k(u') + N}. \quad (\text{A8})$$

2b. Propose to decrease the link variable $m_+ \rightarrow m'_+ = m_+ - 1$: if $m_+ = 0$, then the proposal is rejected, otherwise

$$q = e^{-\mu\nu} \frac{m_+ k'(u) + N}{\beta k'_{12}(u) + 1}. \quad (\text{A9})$$

The acceptance probabilities for moving the $(+)$ end of the worm are described by the same expressions, the case $(+)$, $\pm\hat{\nu}$ is equivalent to $(-)$, $\mp\hat{\nu}$ (both decrease/increase the $Q_{12} = +1$ line by one). However, because of the next updating step, one does not need to move the $(+)$ head to satisfy ergodicity. Due to these facts, in our simulations we did not update the $(+)$ end, but only the $(-)$ end with $2/3$ probability.

3. When the two ends of the worm coincide ($u = v$) it can jump to a new position ($u' = v'$) and change its index.

3a. $(i, i) \rightarrow (j, j)$:

$$q = \frac{(\hat{k}(u) + N)(\hat{k}_j(u') + 1)}{(\hat{k}_i(u) + 1)(\hat{k}(u') + N)} \quad (\text{A10})$$

3b. $(-, +) \rightarrow (-, +)$:

$$q = \frac{(\hat{k}(u) + N)(\hat{k}_{12}(u') + 1)}{(\hat{k}_{12}(u) + 1)(\hat{k}(u') + N)} \quad (\text{A11})$$

3c. $(-, +) \rightarrow (j, j)$:

$$q = \frac{(\hat{k}(u) + N)(\hat{k}_j(u') + 1)}{(\hat{k}_{12}(u) + 1)(\hat{k}(u') + N)} \quad (\text{A12})$$

3d. $(i, i) \rightarrow (-, +)$:

$$q = \frac{(\hat{k}(u) + N)(\hat{k}_{12}(u') + 1)}{(\hat{k}_i(u) + 1)(\hat{k}(u') + N)} \quad (\text{A13})$$

4. Changing the link variables \pm on a given link simultaneously.

4a. $m_+ \rightarrow m'_+ = m_+ + 1, m_- \rightarrow m'_- = m_- + 1$:

$$q = \frac{\beta^2}{m'_+ m'_-} \prod_{x \in \partial l} \frac{k_{12}(x) + 1}{k(x) + N} \quad (\text{A14})$$

4b. $m_+ \rightarrow m'_+ = m_+ - 1, m_- \rightarrow m'_- = m_- - 1$ (if $m_+ = 0$ or $m_- = 0$, then the proposal is rejected):

$$q = \frac{m_+ m_-}{\beta^2} \prod_{x \in \partial l} \frac{k'(x) + N}{k'_{12}(x) + 1} \quad (\text{A15})$$

Note that these expressions with the chemical potential using the modified basis $\phi_+, \phi_-, \phi_3, \dots, \phi_N$ look very similar to those discussed in the case without chemical potential.

-
- [1] E. Y. Loh, J. E. Gubernatis, R. T. Scalettar, S. R. White, D. J. Scalapino and R. L. Sugar, Phys. Rev. B **41** (1990) 9301.
- [2] P. de Forcrand, PoS LAT **2009** (2009) 010 [arXiv:1005.0539 [hep-lat]].
- [3] G. Aarts, Pramana **84** (2015) 5, 787 [arXiv:1312.0968 [hep-lat]].
- [4] G. Aarts, PoS CPOD **2014** (2014) 012 [arXiv:1502.01850 [hep-lat]].
- [5] D. Sexty, PoS LATTICE **2014** (2014) 016 [arXiv:1410.8813 [hep-lat]].
- [6] D. Sexty, Phys. Lett. B **729** (2014) 108 [arXiv:1307.7748 [hep-lat]].
- [7] Z. Fodor, S. D. Katz, D. Sexty and C. Trk, arXiv:1508.05260 [hep-lat].
- [8] A. M. Polyakov, Phys. Lett. B **59** (1975) 79.
- [9] E. Brezin and J. Zinn-Justin, Phys. Rev. B **14** (1976) 3110.
- [10] R. H. Swendsen and J. S. Wang, Phys. Rev. Lett. **58** (1987) 86.
- [11] U. Wolff, Phys. Rev. Lett. **62** (1989) 361.
- [12] F. Niedermayer, Phys. Rev. Lett. **61** (1988) 2026.
- [13] N. D. Mermin and H. Wagner, Phys. Rev. Lett. **17** (1966) 1133.
- [14] S. R. Coleman, Commun. Math. Phys. **31** (1973) 259.
- [15] V. A. Novikov, M. A. Shifman, A. I. Vainshtein and V. I. Zakharov, Phys. Rept. **116** (1984) 103 [Sov. J. Part. Nucl. **17** (1986) 204] [Fiz. Elem. Chast. Atom. Yadra **17** (1986) 472].
- [16] F. Bruckmann, Phys. Rev. Lett. **100** (2008) 051602 [arXiv:0707.0775 [hep-th]].
- [17] G. Parisi and Y. s. Wu, Sci. Sin. **24** (1981) 483.
- [18] G. Parisi, Phys. Lett. B **131** (1983) 393.
- [19] J. R. Klauder, Acta Phys. Austriaca Suppl. **25** (1983) 251.
- [20] J. Ambjorn and S. K. Yang, Phys. Lett. B **165** (1985) 140.
- [21] J. Ambjorn, M. Flensburg and C. Peterson, Nucl. Phys.

- B **275** (1986) 375.
- [22] G. Aarts, F. A. James, E. Seiler and I. O. Stamatescu, Phys. Lett. B **687** (2010) 154 [arXiv:0912.0617 [hep-lat]].
- [23] G. Aarts, E. Seiler and I. O. Stamatescu, Phys. Rev. D **81** (2010) 054508 [arXiv:0912.3360 [hep-lat]].
- [24] G. Aarts, F. A. James, E. Seiler and I. O. Stamatescu, Eur. Phys. J. C **71** (2011) 1756 [arXiv:1101.3270 [hep-lat]].
- [25] G. Aarts, P. Giudice and E. Seiler, Annals Phys. **337** (2013) 238 [arXiv:1306.3075 [hep-lat]].
- [26] E. Seiler, D. Sexty and I. O. Stamatescu, Phys. Lett. B **723** (2013) 213 [arXiv:1211.3709 [hep-lat]].
- [27] H. Makino, H. Suzuki and D. Takeda, arXiv:1503.00417 [hep-lat].
- [28] J. Bloch, J. Mahr and S. Schmalzbauer, arXiv:1508.05252 [hep-lat].
- [29] G. Aarts, L. Bongiovanni, E. Seiler, D. Sexty and I. O. Stamatescu, PoS LATTICE **2013** (2014) 451 [arXiv:1310.7412 [hep-lat]].
- [30] G. Aarts, F. Attanasio, B. Jger, E. Seiler, D. Sexty and I. O. Stamatescu, PoS LATTICE **2014** (2014) 200 [arXiv:1411.2632 [hep-lat]].
- [31] G. Aarts and F. A. James, JHEP **1008** (2010) 020 [arXiv:1005.3468 [hep-lat]].
- [32] N. Prokof'ev and B. Svistunov, Phys. Rev. Lett. **87** (2001) 160601.
- [33] U. Wolff, Nucl. Phys. B **810** (2009) 491 [arXiv:0808.3934 [hep-lat]].
- [34] D. Banerjee and S. Chandrasekharan, Phys. Rev. D **81** (2010) 125007 [arXiv:1001.3648 [hep-lat]].
- [35] Y. D. Mercado, H. G. Evertz and C. Gattringer, Comput. Phys. Commun. **183** (2012) 1920 [arXiv:1202.4293 [hep-lat]].
- [36] K. Langfeld, Phys. Rev. D **87** (2013) 11, 114504 [arXiv:1302.1908 [hep-lat]].
- [37] Y. Delgado, C. Gattringer and A. Schmidt, PoS LATTICE **2013** (2014) 147 [arXiv:1311.1966 [hep-lat]].
- [38] E. V. Herland, T. A. Bojesen, E. Babaev and A. Sudbo, Phys. Rev. B **87** (2013) 13, 134503 [arXiv:1301.3142 [cond-mat.stat-mech]].
- [39] C. Gattringer, T. Kloiber and M. Mller-Preussker, arXiv:1508.00681 [hep-lat].
- [40] L. P. Yang, Y. Liu, H. Zou, Z. Y. Xie and Y. Meurice, arXiv:1507.01471 [cond-mat.stat-mech].
- [41] F. Bruckmann, C. Gattringer, T. Kloiber and T. Sulejmanpasic, Phys. Lett. B **749** (2015) 495 [arXiv:1507.04253 [hep-lat]].
- [42] F. Bruckmann, C. Gattringer, T. Kloiber and T. Sulejmanpasic, arXiv:1509.05189 [hep-lat].
- [43] S. Caracciolo, R. G. Edwards, A. Pelissetto and A. D. Sokal, Nucl. Phys. B **403** (1993) 475 [hep-lat/9205005].
- [44] D. Negradi, JHEP **1205** (2012) 089 [arXiv:1202.4616 [hep-lat]].
- [45] S. Caracciolo, R. G. Edwards, A. Pelissetto and A. D. Sokal, Nucl. Phys. Proc. Suppl. **42** (1995) 752 [hep-lat/9411064].
- [46] S. Caracciolo, R. G. Edwards, A. Pelissetto and A. D. Sokal, Phys. Rev. Lett. **75** (1995) 1891 [hep-lat/9411009].
- [47] J. Balog, M. Niedermaier, F. Niedermayer, A. Patrascioiu, E. Seiler and P. Weisz, Phys. Rev. D **60** (1999) 094508 doi:10.1103/PhysRevD.60.094508 [hep-lat/9903036].
- [48] Z. Fodor and S. D. Katz, Phys. Lett. B **534** (2002) 87 [hep-lat/0104001].
- [49] Z. Fodor, S. D. Katz and K. K. Szabo, Phys. Lett. B **568** (2003) 73 [hep-lat/0208078].
- [50] F. Csikor, G. I. Egri, Z. Fodor, S. D. Katz, K. K. Szabo and A. I. Toth, JHEP **0405** (2004) 046 [hep-lat/0401016].
- [51] G. G. Batrouni, G. R. Katz, A. S. Kronfeld, G. P. Lepage, B. Svetitsky and K. G. Wilson, Phys. Rev. D **32** (1985) 2736. doi:10.1103/PhysRevD.32.2736
- [52] G. Boyd, J. Engels, F. Karsch, E. Laermann, C. Legeland, M. Lutgemeier and B. Petersson, Nucl. Phys. B **469** (1996) 419 doi:10.1016/0550-3213(96)00170-8 [hep-lat/9602007].
- [53] E. Seel, D. Smith, S. Lottini and F. Giacosa, JHEP **1307** (2013) 010 doi:10.1007/JHEP07(2013)010 [arXiv:1209.4243 [hep-ph]].
- [54] A. Mollgaard and K. Splittorff, Phys. Rev. D **88** (2013) 11, 116007 doi:10.1103/PhysRevD.88.116007 [arXiv:1309.4335 [hep-lat]].
- [55] A. Mollgaard and K. Splittorff, Phys. Rev. D **91** (2015) 3, 036007 doi:10.1103/PhysRevD.91.036007 [arXiv:1412.2729 [hep-lat]].